Galaxy evolution in poor clusters

Amaya Gaztelu

Galaxy Evolution in Poor Clusters

by Amaya Gaztelu

A Thesis submitted to the University of Durham
in accordance with the regulations for
admittance to the Degree of Master of Science.

Department of Physics
University of Durham
December 2000

Abstract

We study the galaxy population in poor clusters and compare it with the existing results for rich clusters, in an attempt to understand the role of the environment in the formation and evolution of galaxies.

Studies of rich clusters of galaxies have revealed dramatic transformations between the population of local and distant clusters. Specifically, distant rich clusters have a higher fraction of blue galaxies and significantly less S0 galaxies than their local counterparts. The effectiveness of the candidate mechanisms responsible for these transformations depends on the density of the environment. Our aim is to try to distinguish between these mechanisms.

This thesis is part of a larger project comprising of a sample of nine X-ray selected poor clusters in the redshift range 0.2-0.3. These data comprise of ground based photometry, multi-slit spectroscopy and HST images. This work concentrates on four of the nine clusters of the sample. We have obtained Colour-Magnitude Diagrams for these clusters and calculated their blue galaxy fraction. We find values similar to those found for rich clusters at similar redshifts. We also show results from the morphological analysis of the HST images, performed as a side project to this work. The morphological analysis reveals that our clusters have a higher fraction of low B/T systems than rich clusters.

We discuss the different candidate mechanisms and argue that the so-called "strangulation" is the only one compatible with our findings. In this scenario, galaxies loose their gas envelope as they are accreted to the cluster and star formation is gradually truncated as the galaxy consumes the rest of its gas. This process does not have a significant effect on the morphology of the infalling galaxy. In rich clusters, where other mechanisms (tides, harassment, ram-pressure stripping) are effective, the morphology of the galaxy will be transformed.

Contents

List of Figures

List of Tables

Preface

The work described in this thesis was carried out between October 1999 and December 2000, while the author was a research student under the supervision of Professor R. L. Davies and Dr R. G. Bower in the Department of Physics at the University of Durham. This work has not been submitted for any other degree at the University of Durham or at any other University.

Part of this work has ben done in collaboration with R.L Davies, R. Bower, M. Balogh, I. Smail, B. Ziegler and T. Kodama.

Acknowledgements

Here it is where I have the chance to thank the people that helped me in making this "little book" possible.

I want to thank my supervisor, Roger Davies, because it is thanks to him that I came to Durham and this "book" became true. I would like to give a big thanks (a very big one) to Richard Bower, who helped and supported me in many ways. A big thanks goes also to Mike Balogh, for being always there to answer all my (silly) questions. I also want to thank other collaborators: "Taddy" Kodama, Ian Smail and Bodo Ziegler for their help in this work.

Thanks to the people in room 129 (Fiona, Rich, Dave, Kevin and Dajana).. it was fun arguing with you all (and singing and dancing and .. working as well!). Thanks for standing my grumpy mood while I was writing this.

Big thanks to my non-astronomer friends in Durham (specially to Katie, Michele and Katy) for keeping me "sane", for the long chats in the kitchen, and for "pushing" me to do what I was not brave enough to do (about fish)!

Thanks to the "squash dinner club" (Chris, Rich and Peder), squash was an excuse, what I really enjoyed was those dinners and the long conversations that usually followed.

Of course, a very special thanks to P. Merriweather, for everything. For the invitation to Mexico, and the purple goblins, and the red curl and the letters to read upside-down. Or simply just for being, and making life in colour. Gracias Prudence por hacer la vida en color.

A special thanks to my parents who supported me in all what the word means. Muchas gracias (Ofe y Nacho) por estar siempre ahí, por entender mi decisión y apoyarme en todo momento. Este "libro" no hubiera sido posible sin vosotros. (...ah, y gracias por la caja de polvorones que ayudó a la recuperación post-tesis!!)

And last but not least, thanks to Mikey for... for being Mikey!

A very big thanks to all of you who understood my decision of "changing the path of my life" and who supported me in taking it. Gracias.

To those who understood that:

Caminante, no hay camino,
se hace camino al andar.

Antonio Machado

Chapter 1 | *Introduction*

Clusters of galaxies are the largest bound systems in the Universe. They contain a high density of galaxies and a large amount of gas which is compressed and heated in the deep cluster potential well, so that it emits at X-ray wavelengths. As early as 1865, astronomers had already observed that galaxies (or "nebulae" as they were called at that time) were not uniformly distributed in the sky, but showed a tendency to be arranged in groups, ranging from pairs to large clusters of thousands of nebulae (Wolf 1865). For decades, clusters of galaxies were thought without question to be stationary systems and the first calculations for the mass of clusters assumed a relaxed state (Zwicky 1937, Smith 1936). However, signs against the relaxed state of clusters began to appear in the late 1950's when Zwicky observed a different distribution of ellipticals and spirals in the Virgo cluster (Zwicky 1957). This, together with the finding of higher velocity dispersion of spirals relative to ellipticals (de Vaucouleurs 1961, Sandage and Tammann 1976), is not consistent with a stationary structure, where velocity dispersion should decrease with radius. Since then, evidence for the evolution of clusters has been growing from the morphological and kinematical differences between galaxies in different parts of clusters, observations of different degrees of subclustering and the different properties of galaxies in distant and local clusters. The conclusion from these observations is that clusters are not in a stationary state but are still in the process of forming.

The first catalogues of clusters were created by visual inspection of photographic plates. Abell (1958) and Zwicky (1968) produced the first catalogues, where clusters were defined (Abell 1958) as an overdensity of galaxies within a radius around a centre. The catalogues were classified to reflect on their apparent magnitude and their "richness" (overdensity). The first X-ray survey of the sky in the 1970's (UHURU satellite) showed that the rich nearby clusters are X-ray sources and a decade later it was demonstrated that clusters of galaxies up to redshifts of 0.5

are bright X-ray sources with luminosities in the range $10^{42} erg\ s^{-1}$ to $10^{45} erg\ s^{-1}$. Consequently X-ray surveys have been used to detect and catalogue clusters of galaxies.

Clusters of galaxies are important in testing models of galaxy evolution in dense regions. The fact that galaxy properties are different in clusters and the field was observed as early as the 1930's (Hubble and Humanson, 1931). Since then it has been clear that the environment is linked with the formation and evolution of galaxies, but the relation is not yet well understood and remains as one of the open questions in galaxy evolution. The evolution of galaxies in poor clusters is a crucial point in our understanding of the role of the environment in the formation and evolution of galaxies. During the past years there have been extensive studies of rich clusters of galaxies, but are the properties found here applicable to galaxies in poor clusters?

In this thesis I will review the relevant topics on evolution of galaxies in clusters, paying special attention to the effect of the environment. I will also describe my thesis project, whose aim is to compare the evolution of galaxies in poor clusters with the existing results for rich clusters, in an attempt to understand how these different environments affect the evolution of galaxies.

1.1 General properties

The properties of galaxies in local (present day) clusters differs with those in distant clusters. Galaxies in local clusters show homogeneity in their properties, which reflects a uniformity in their formation (Bower, Lucy and Ellis 1992). However, the increasing activity seen as a function of redshift implies different formation histories for galaxies in distant clusters. The population of blue star forming galaxies observed in distant clusters contrasts to the red homogeneous population of local clusters, whose properties indicate a long period of passive evolution. We will discuss these properties (such as the Colour Magnitude Relation and the Fundamental Plane), but first we will review the general models of galaxy formation.

There are two general models of galaxy formation: the Classical model (Larson

1975, Arimoto and Yoshii 1987) and the Hierarchical model (Cole et al. 1994, White and Frenk 1991). The main difference between the two models is that in the Classical model, morphology is set at an early time, whilst in the Hierarchical model the morphology can change as a result of a rearrangement after each merger.

In the Classical model, star formation is initially rapid after the collapse of gas clouds (Arimoto &Yoshii 1987). When massive stars in the protogalaxy reach the supernova phase there is a competition between the gravitational potential, which tends to retain the gas, and the supernova winds which tend to expel it. Therefore, star formation can continue longer in massive systems which leads to a higher mean metal abundance. If the galaxy is in a cluster the material is lost to the intracluster medium, but if the galaxy is isolated a gas disc can be formed from the expelled material and star formation can continue in a quiescent mode.

In the Hierarchical picture, mergers of gas clouds induce star formation and stars are redistributed into an spheroid. A disc can appear if more gas is accreted. In this sense the morphology is not fixed and can vary depending on how many and how strong the mergers are.

Fundamental relations like the "Colour Magnitude Relation" (CMR) and the "Fundamental Plane" (FP) can be used to study the formation history of galaxies in clusters.

The "Fundamental Plane" (Djorgovski & Davis 1987) is a relation between the effective radius r_e, effective surface brightness μ_e and velocity dispersion σ of early-type galaxies, of the form $r_e \propto \sigma^{1.25}\mu_e^{0.8}$. The measured values of r_e, μ_e and σ are limited to a thin plane by this relation, and show a small scatter. The existence of the FP can be interpreted as a consequence of the virial theorem and also as a relation between the mass and the mass to light (M/L) ratios of galaxies ($M/L \propto M^{0.2}$) and can be used to study the evolution of galaxies with redshift. The results of studies of the FP at different redshifts (Jørgensen et al. 1999) put a limit on the redshift at which the majority of stars were formed, having to be greater than $z \sim 2$. This is done by studying the change in the zero point of the FP with redshift, which under the assumption of passive evolution, is equivalent to the evolution of the M/L ratio. The M/L ratio evolves because as the galaxy ages the luminosity

decreases (this is often referred to as passive evolution). Although assuming passive evolution is a simplified view, this procedure puts limits on the redshift at which the bulk of the star formation occurred.

The existence of a linear trend in the Colour Magnitude Diagram (CMD), where the colours of elliptical galaxies are bluer for fainter magnitudes, is a main characteristic of the galaxy population of clusters. The Colour Magnitude Relation is well defined and shows very low scatter for early-type galaxies. The CMR at the present epoch can be explained either as a metallicity effect or as an age effect, but when the evolution of this relation with redshift is taken into account the age hypothesis is rejected. This is because if the CMR was an age effect it should not exist beyond a certain look-back time when the formation epoch of faint galaxies is being approached. But observations of distant clusters show that the CMR already exists at higher redshifts. Evolutionary models (Kodama and Arimoto 1997) confirm that the slope of the CMR can be explained as a metallicity effect, while the scatter in the relation is due to variations in age. In this picture ellipticals are primarily old, with the bulk of star formation occurring at $z > 2$ and wind feedback being responsible of the mass-metallicity relation (massive galaxies can retain more gas becoming more metal enriched). Alternatively the mass-metallicity relation can be explained in the hierarchical model of galaxy formation (White and Frenk, 1991) by considering that star formation is enhanced in the merger process of formation of more luminous ellipticals and that less of this gas is stripped from the system so the result is a higher metallicity.

As mentioned before, the CMR exists even for the most distant clusters studied(Stanford et al. (1997) finds a CMR for a cluster at z =1.27), but the surprising result was the increase in the fraction and magnitudes of blue galaxies in high redshift clusters. This is the so called Butcher-Oemler effect, which will be discussed in more detail later. Models in which the bulk of the stellar population is old, but in which star formation is allowed to continue in some galaxies until recent times, can explain both the low scatter of the CMD of local clusters and the blue galaxy fractions observed in intermediate redshift clusters (Bower, Kodama & Terlevich 1998).

A comparison of the CMR of clusters at different redshifts is shown in figures 1.1 and 1.2 where it can be seen how the number of galaxies lying blueward of the ridgeline increases with redshift.

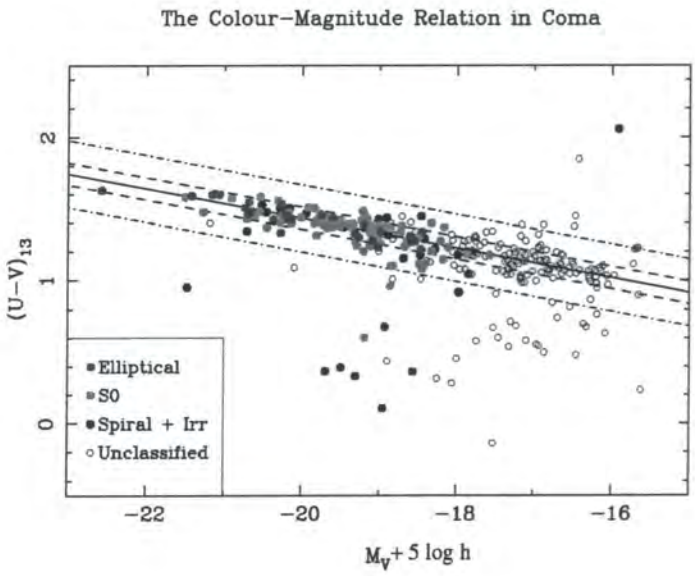

Figure 1.1: CMR for the Coma cluster, Terlevich et al. (1999).

1.2 Butcher-Oemler Effect

The first results of Butcher and Oemler in 1978 and 1984 (BO84) had a big impact on the view of galaxy evolution in clusters. Butcher and Oemler studied 33 clusters of galaxies between z=0.003 and z=0.54 and established that the fraction of blue galaxies in clusters has a dramatic increase with redshift. But galaxies can not escape from clusters, so the population observed in distant clusters has to evolve into the population observed in present day local clusters. Since the original work of Butcher and Oemler, many studies have been carried out in order to confirm their findings, and although the trend is generally accepted there is still controversy about the degree of the increase of the blue fraction of galaxies with redshift.

The evolution of the colours of galaxies in clusters in known as the "photometric Butcher-Oemler (BO) effect".

The original work of Butcher and Oemler was performed using only photometry

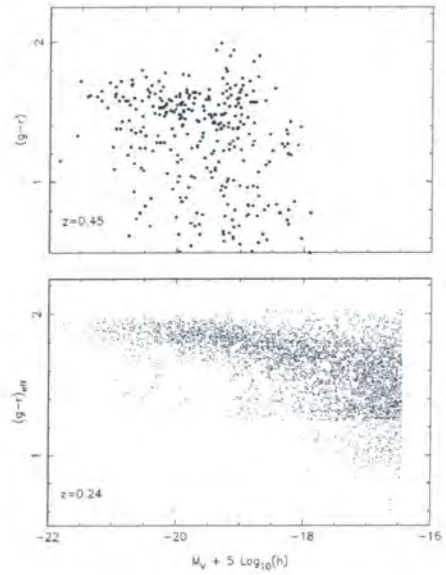

Figure 1.2: CMR for clusters at different redshifts, z=0.45 (top panel) Dressler et al. (1997); z=0.24 Smail et al. (1998). The magnitude and number of galaxies lying blueward of the ridgeline increases with redshift, compare also with the previous figure for Coma.

of the galaxies in the sample, a few years later the first spectroscopic studies of the blue galaxies also brought surprising results (Dressler and Gunn 1983, Lavery and Henry 1986, Couch and Sharples 1987). These studies showed that many of the blue BO galaxies had strong Balmer lines compared to local galaxies, but had no emission lines (this new type of galaxy was called post-starburst, since these kind of spectra are produced when star formation has been abruptly truncated). The increase of this spectral class with redshift is known as "the spectroscopic Butcher-Oemler effect".

There is also what we could call the "morphological Butcher-Oemler effect", ie the evolution of the galaxy morphologies with redshift. This became apparent when images from the *Hubble Space Telescope* (HST) allowed a morphological classification of galaxies in distant clusters, revealing that the fraction of S0 galaxies in rich clusters decreases with redshift (Dressler et al. 1997).

The reason for separating these three "different" effects is that although several attempts have been made to relate the photometric, spectroscopic and morphological trends, it is not clear that they are due to the same cause. All these topics will

be discussed in the following sections; but I will now concentrate in the photometric BO effect.

In order to calculate the blue fraction of galaxies in a cluster we need to define what a "blue" galaxy is, the general approach is to use the definition that BO introduced. In this way "blue" galaxies are those with a B-V colour in the rest frame lying at least 0.2 magnitudes below the red sequence, and within R_{30} (the radius from the cluster center that contains 30 percent of the cluster population). The blue fraction in the original BO84 sample was negligible in clusters with redshift $z < 0.1$ ($f_b \sim 0.03$) and reached 0.25 at z=0.5. Many studies have been carried out to investigate this increase with redshift of the blue fraction of galaxies in clusters, but as yet there is no consensus.

An example of this can be seen in figure 1.3, where the original BO84 data is compared to data from Rakos and Schomber 1995, Margoniner and Carvalho 2000 and Smail et al. 1998. Rakos and Schomber (1995) studied a sample of rich clusters in the redshift range z=0.4 to z=0.9 and found a steeper relation than BO84, with an increase from 20% at z=0.4 to 80% at z=0.9, this would indicate even stronger evolution than previously suggested. The data from Margoniner and Carvalho (2000) (consisting of 44 Abell clusters) shows a relation closer to that of Rakos and Schomber (1995). On the other hand Smail et al. (1998) sample, which consist of 10 clusters at z=0.22-0.28, gives a fraction of blue, star-forming galaxies of only 5%. The advantage of Smail et al.'s study is that it has been X-ray selected in order to contain the richest clusters at that redshift. As a result it can be easily compared to the richest local clusters. Although the fraction of blue galaxies is low in this sample, it has to be mentioned that the values for individual clusters show a large scatter and that the value does not correlate with the concentration of the cluster or the X-ray morphology.

Other authors find different results than Smail et al. (1998) also using X-ray selected bright clusters. Kodama and Bower (2000) selected 7 CNOC* clusters in the redshift range z=0.23-0.43 with X-ray luminosities $L_X = 4 - 28 \times 10^{44} erg\ s^{-1}$, and found an evolution of the blue fraction which fits remarkably well the original trend

*CNOC: Canadian Network for Observational Cosmology Cluster Survey; Yee, Ellingson and Carlberg (1996).

from BO84 as can be seen in figure 1.4. These authors apply a colour dependence correction to the magnitude cut and indicate that the original definition of the magnitude cut from BO84 tends to overestimate the blue fraction, but even after applying this correction the Kodama and Bower data shows an evolution similar to BO84. (see figure 1.4). The Smail et al. (1998) and Kodama & Bower (2000) samples have one cluster in common (A2390) and although Smail et al. (1998) value for f_b in this cluster is smaller, the results are consistent at the 1 σ level.

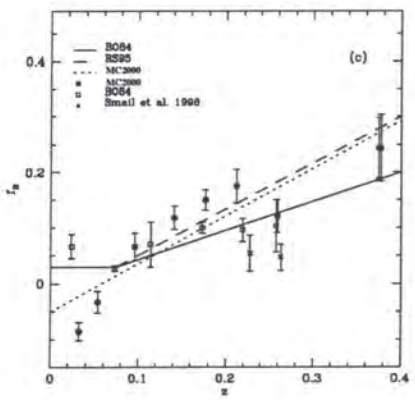

Figure 1.3: Evolution of blue fraction with redshift. □ is the Butcher and Oemler (1984) data. • is data from Margoniner and Carvalho (2000), × is Smail et al. (1998). The solid and dashed lines represent the relation originally found by BO84 and the one by Rakos and Schomber 1995 respectively.

The discrepancy between samples clearly shows the need for an unbiased selection criteria. There have been suggestions of strong biases in the selection of clusters in the BO84 sample, indicating that it is made of different kind of objects at different look-back times. This would imply that the evolution of the blue fraction cannot be traced using this sample, and that the Butcher-Oemler effect could be in part only a selection effect (Andreon and Ettori 1999). In order to interpret and compare results it is therefore crucial to have well defined samples.

Another question concerning the blue galaxies is their spatial distribution within the cluster. In a widely accepted scenario, galaxies are continously accreted from the field and we would expect the occurrence of blue galaxies to be larger in the outskirts of the cluster. This was found in the BO84 sample, where the blue fraction

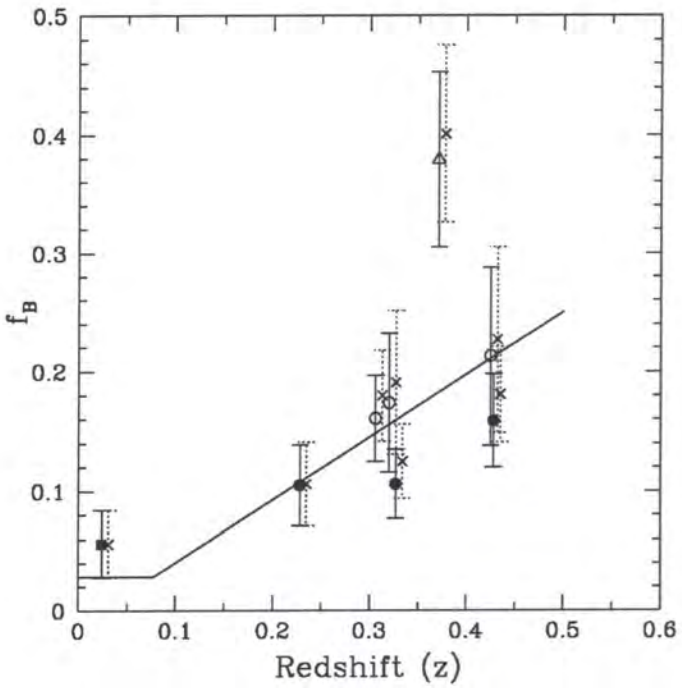

Figure 1.4: Blue galaxy fraction from Kodama & Bower (2000) data. Open circles are clusters for which R_{30} could not be directly calculated due to small spatial coverage. Crosses are the values not taking into account the corrections for the magnitude cut. The Coma cluster is represented by the filled square and the triangle is a cluster thought to be contaminated by a foreground group. The line shows the original BO84 result.

increases with projected radius for nearby and distant clusters. Morris et al. (1998) studied this topic in cluster MS1621.5 (z=0.427) and found that the blue fraction increases until it reaches the field value. Similar trends are observed in Kodama & Bower (2000) for their sample of 7 CNOC clusters. Actually, this reflects the morphology-radius relation (TR) found by Dressler in 1997: the fraction of spiral galaxies increases with radius in the cluster. Assuming that the blue fraction and the spiral fraction are directly related (this will be discussed later as well as the morphology density relation) it is possible to compare the morphology-radius relation and the radial dependence of f_b. This has been done by Kodama & Bower (2000) and as can be seen in figure 1.5 the slope of the T-R relation at different redshift can explain the radial dependence of f_b.

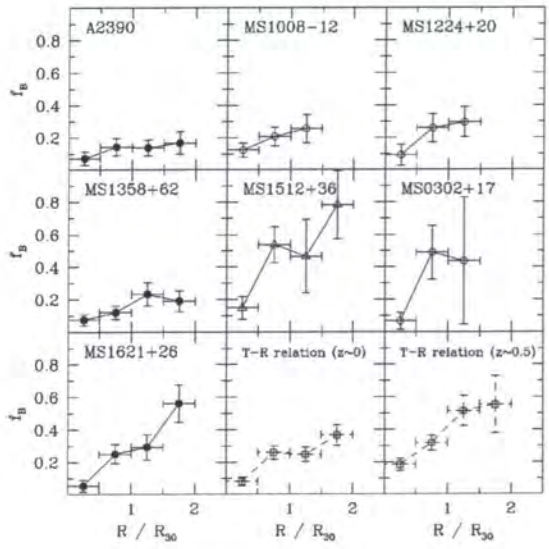

Figure 1.5: Radial dependence of the blue fraction of galaxies for 7 CNOC clusters, from Kodama & Bower (2000). Also the T-R relations from Dressler et al. 1987 are plotted in the last two panels.

1.3 Spectroscopic Studies

After the first results suggesting an evolution with redshift in the colours of galaxies in clusters, the next step was to confirm that the blue galaxies were indeed cluster members, and therefore with this aim spectroscopic studies were undertaken

(Dressler & Gunn 1983, Lavery & Henry 1986, Couch & Sharples 1987 are some of the first ones). These studies did confirm the membership of the blue galaxies and also yield an unexpected result showing that many of the blue galaxies and some red ones exhibit strong Balmer absorption lines but do not have emission lines.

This kind of spectrum indicates that the galaxy does not have on-going star formation (no emission lines), but was forming stars recently in the past. Strong Balmer emission can only be reproduced by models where the star formation was abruptly truncated after a starburst. This is the reason for which these galaxies are referred to as "post-starburst" (PSB), or "E + A" (Dressler & Gunn 1983), and although they exist in local galaxy samples, their occurrence and their activity seems to be lower than in distant clusters (Caldwell & Rose 1997). The star formation properties of galaxies have also been compared between rich clusters and the field. On average galaxies in the field have star formation rates (SFR) higher than galaxies in the cores of rich clusters and there is a gradient of the star formation rate inside the cluster from lower values to values reaching the field SFR values.

But this is still an open question, and attempts to determine the fraction of passive, star-forming or post-starburst galaxies in clusters carried by different authors yield very different results. The most important differences are found between the CNOC and the MORPHS collaborations. Balogh et al. (1999) analyse fifteen clusters from the CNOC sample in the range z=0.18 - 0.55, and show a small increase in the fraction of star forming galaxies with redshift. The same study shows that the fraction of galaxies with strong absorption lines (Hδ) and no [OII] emission (here called K+A) does not increase significantly with redshift, and it is never significantly in excess compared to the field value, at any radius in the cluster. But a similar study by the MORPHS collaboration, based on a sample of eleven clusters at z=0.37 - 0.56 published shortly after Balogh's study (Dressler et al. 1999, Poggianti et al. 1999), concludes that the occurrence of K+A galaxies in clusters is significantly higher than in the field and that their frequency in clusters is higher at z=0.4-0.5 than at low redshift. Poggianti et al. (1999) also identify galaxies with strong absorption and also [OII] emission lines, which are numerous in both the field and clusters at high redshift. They call these galaxies "dusty starbursts" and suggest that their star formation is underestimated due to extinction and they

could be the progenitors of the post starburst population in distant clusters.

The scenarios inferred from the different results outlined above, are therefore different. Balogh et al. (1999) conclude from their results that the cluster environment is not responsible for inducing starbursts, and that the truncation of the star formation in clusters is a gradual process caused by the exhaustion of the gas in the disc. They suggest that field galaxies can regenerate their star formation by refueling their discs with gas from a halo, while galaxies in clusters do not have such a halo and evolve passively. On the other hand many authors claim that the presence of K+A galaxies is evidence of recent strong starbursts in a large percentage of the cluster galaxies (Couch et al. 1998, Poggianti et al. 1999) and suggest that the suppression of star formation is not a gradual but an abrupt process after the galaxies are accreted to the cluster.

The possible causes for this disagreement are discussed in Balogh et al. (1999) and Ellingson et al. (2000), including the cluster selection, the galaxy selection and galaxy classifications used by the CNOC and MORPHS collaborations. The authors point out that the systematic differences between the samples can be due to the different selection techniques. The CNOC sample is an X-ray selected sample while the MORPHS sample is composed of optically and AGN-selected clusters.

The origins of gradients in star formation rates in rich clusters are investigated in Balogh et al. (2000). These authors conclude that they are consistent with the scenario mentioned above (Balogh et al. 1999), where the truncation of star formation is a gradual process which takes a few Gyrs so the gradients are caused by the time passed since accretion. Kodama & Bower (2000) also analyse this problem. They find that models where the effect of the cluster is to remove the halo of the galaxy so the star formation is "suffocated", and the remaining gas is consumed on a timescale of 1 Gyr, can reproduce better the observed colour distributions for galaxies in clusters than models where star formation is abruptly truncated after a strong burst. At the same time, the former models reproduce better the fraction of Hδ strong and [OII] emission galaxies given by the CNOC group than the one by the MORPHS group.

The evolution of colours and star formation rates in clusters have been also

studied in the context of hierarchical galaxy formation (Diaferio et al. 2000). These models support the scenario inferred from the CNOC observations, with a gradual decline of the star formation and no starburst after the galaxy is accreted to the cluster.

An important role could be played by dust obscuration, which would tend to underestimate the star formation rates because most spectroscopic surveys use [OII] as the indicator of star formation, which is quite sensitive to dust extinction. In order to avoid this problem, there are currently projects to use Hα as an indicator of star formation, since it is less sensitive to obscuration than [OII]. But the first results from Balogh & Morris (2000) for A2390 show that there is no evidence of strong star formation in this cluster and that the number of Hα emitters is not significantly higher than the [OII] emitters, with similar radial distributions. The authors conclude that these results support the strangulation model of cluster galaxy evolution suggested from the CNOC survey, and shows that cluster induced star formation does not play an important role in galaxy evolution in clusters.

1.4 Morphological Evolution

One further step in understanding the origin of the transformation of the galaxy population in clusters, is to relate the evolution of the stellar population to the evolution of the galaxy morphology. The first attempts to study the morphology of galaxies in clusters at $z \geq 0.2$ came from ground based images by Thompson (1986, 1988) and Lavery & Henry (1988) and although the samples were small they suggested that many of the blue galaxies were in interacting systems and showed spiral structure. Subsequently, studies using high resolution images (Lavery, Pierce & McClure 1992, Lavery & Henry 1994) reported that a significant fraction (~50%) of the blue galaxies were disc systems, most of which are late-type systems and ~40-45% of them are interacting and/or mergers.

But due to the Hubble Space Telescope the morphology of galaxies in distant clusters has been determined with accuracy surpassing many local clusters. This has revealed significant differences between the morphological properties of galaxies in nearby and distant clusters.

The largest study of this kind using HST has been done by the MORPHS group (10 clusters at z=0.37-0.56), and has yielded classifications for thousands of galaxies. The blue galaxies (star forming and post starburst) have been identified in their majority as spirals (Poggianti et al.1999, Dressler et al. 1999) and a large proportion of them show disturbed morphologies.

Regarding the fractions of different morphological types at different redshifts, it seems clear that rich clusters at intermediate redshifts have significantly less S0 galaxies than their local counterparts, whilst there is an overabundance of spirals in the cores of clusters at z=0.3-0.5. Furthermore, the fraction of ellipticals remains almost constant (Dressler et al. 1997, Smail et al. 1997). Therefore, the bright ellipticals seem to have been in place in the cores of rich clusters since z$\sim$0.6 without much change, while the disc galaxy population seems to be strongly affected by the cluster environment.

There are only three clusters at redshift greater than 0.6 for which morphological studies have been performed. Lubin et al. (1998) find a high fraction of early type galaxies for a cluster at z=0.9, and a low fraction for a cluster at z=0.8. Van Dokkum et al. (2000) report a low fraction of early type galaxies in a z=0.83 cluster. The number of studies at these redshifts is currently too small to draw any firm conclusions.

Another question regarding galaxy morphology is the morphology-density relation (MD) found by Dressler (1980) in all types of clusters at low redshift. This is a correlation between the galaxy morphology and the projected local density of galaxies where, as the local galaxy density increases, the fraction of ellipticals increases and the fraction of spiral decreases. Dressler found (1997) that the MD relation holds for high concentration regular clusters at z$\sim$0.5, but not for low concentration irregular clusters at this redshift, as it can be seen in figure 1.6.

Further studies of the morphological fractions related to the cluster morphology have been done. Fasano et al. 2000 derive morphologies for galaxies in nine clusters in the redshift range $0.1 \leq z \leq 0.25$, and find a large scatter in the S0/E ratio which is related to the cluster morphology. Clusters with a high concentration of ellipticals in their cores (HEC clusters) present a lower S0/E ratio than clusters where the distribution of ellipticals is more uniform (LEC clusters) (figure 1.7). The trend

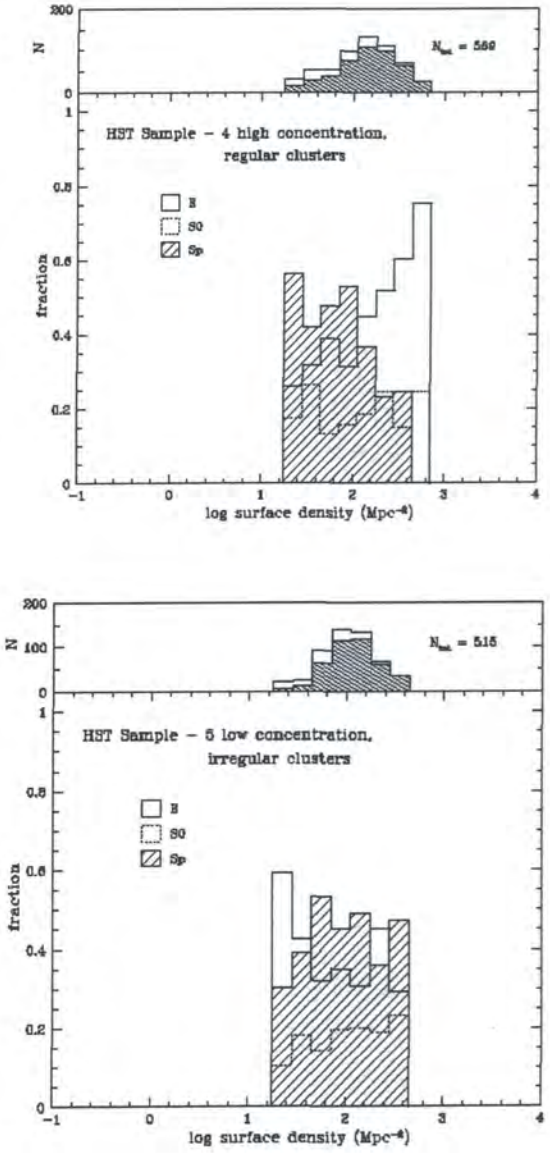

Figure 1.6: Fraction of the different morphological types as a function of local density for high and low concentrated clusters from Dressler at al. (1997) (clusters at intermediate redshift).

with redshift previously found is confirmed here: as redshift increases the S0 fraction decreases and the spiral fraction increases, while the elliptical fraction does not show a trend with z. This intermediate redshift sample shows morphological fractions intermediate between other high and low redshift data, showing that the change in morphological abundances is a continuous one.

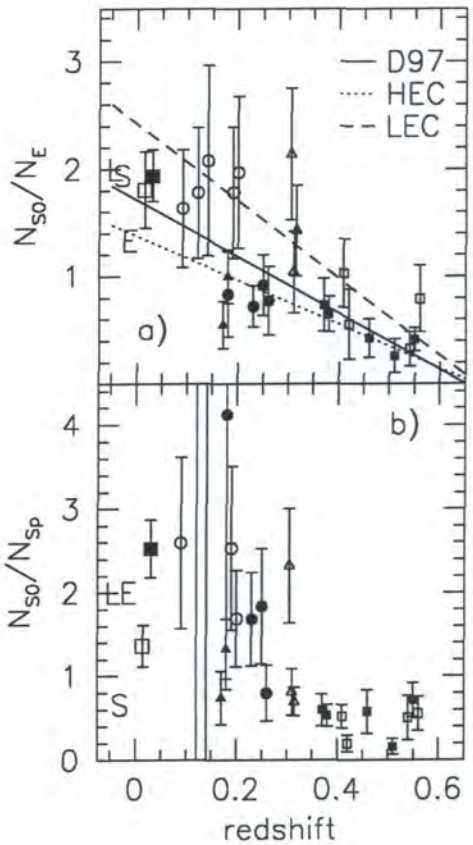

Figure 1.7: Evolution of the S0/E and S0/Sp ratios from Fasano et al. (2000). Solid symbols are for HEC clusters and open symbols for LEC clusters. Circles are data from Fasano et al. (2000), squares are MORPHS data and triangles Couch et al. (1998) data. Dotted and dashed lines are the least square fits for the HEC and LEC clusters and the solid line represents the relation for the MORPHS data.

Fasano et al. (2000) also examine the MD relation and find that it only exists at z ~0.1-0.2 for the high concentration clusters, as found at higher redshift in the Dressler et al. (1997) sample (at $z = 0.5$). Since this relation exists for all clusters at z=0, the authors suggest that the MD relation in low concentration clusters was

established in the last 1-2 Gyr.

Attempts to correlate the photometric, spectroscopic and morphological features have been made. It is generally accepted that most of the blue galaxies responsible of the photometric BO effect, are spirals and that the rest have disturbed morphologies due to interactions or mergers. Poggianti et al. (1999) try to relate morphology and spectroscopy characteristics, and point out that the fact that post-starburst galaxies show spiral morphology rather than S0 morphology, indicates that either the timescale or the process causing the truncation of the star formation and the one responsible for the morphological transformation are different. They also find that at z$\sim$0.5 galaxies with strong absorption and [OII] emission (dusty starbursts) can be clearly related to mergers/interactions in half of the cases, and that cluster members with strong [OII] emission are in most cases late-type galaxies.

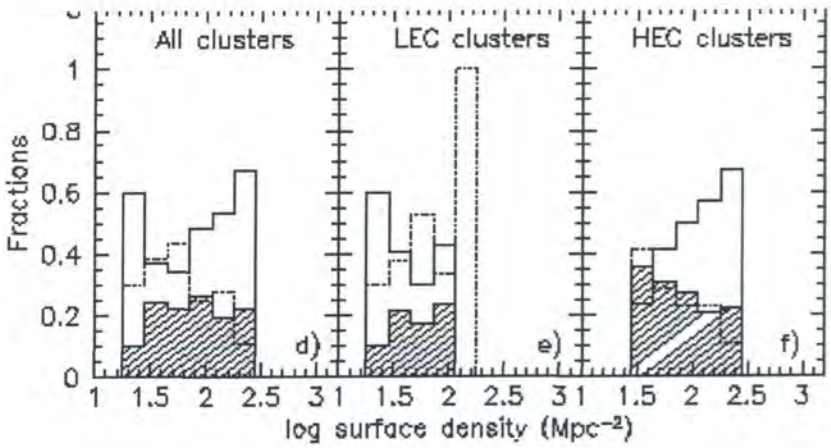

Figure 1.8: Fraction of galaxies of different morphological types for HEC and LEC clusters from Fasano et al. 2000 (sample at z=0.1-0.2). Solid line is for ellipticals, dotted line for S0's and shaded histogram for spirals. Compare with the high redshift distributions in figure 1.6 .

1.5 Mechanisms

Different mechanisms have been suggested to explain the transformation in the cluster populations with redshift and between clusters and the field. We will give a brief description of these processes here and will discuss them in more detail in

chapter 5 in the context of our results.

One possibility is that the blue Butcher-Oemler (BO) galaxies are field galaxies infalling in the cluster and that ram pressure from the intracluster medium (ICM) removes the gas component from the discs, altering the morphology and star formation of the accreted galaxies (Gunn & Gott 1972). This explains the observational fact of blue galaxies being more abundant in the outskirts of the clusters. Hydrodynamical 3-D simulations of the stripping process (Quilis et al. 2000) show that ram pressure can remove the gas component of a spiral galaxy as it moves through the ICM, thereby halting star formation, and eventually transforming a spiral into an S0.

Another suggestion is that the blue BO galaxies originate from galaxy-galaxy interactions, but it seems that there are not enough of these mergers to explain the BO effect. This is because the probability of mergers is low in the dense environments of clusters due to the high relative velocity of the interacting galaxies compared to their internal velocities (Ghigna et al. 1998). Another kind of interaction, the so-called galaxy harassment (high speed close encounters between the infalling spiral and clusters galaxies), has also been shown through simulations to be able to account for the morphological transformations of faint spirals into spheroidals (Moore et al. 1996).

It has also been suggested that the BO effect is a reflection of a hierarchical model for the formation of clusters, and the mergers of subclusters induces star formation by producing shocks in the ICM. Kauffmann (1995) suggests that subclustering was more common in the past which would therefore explain the BO effect. Studies of clusters with different levels of substructure support this explanation (Caldwell and Rose 1997) finding that clusters with a higher degree of substructure tend to have higher fraction of blue galaxies.

All the above processes are plausible, but there is still a debate about the actual changes that each scenario would produce in the galaxy population. Although these changes could be tested observationally, there are also important contradictions in the observations as it has been discussed earlier (see Section 1.3).

For example, an initial burst followed by an abrupt truncation of the star formation is required to explain the high fraction of post-starburst galaxies observed

by the MORPHS group. However, a gradual decline in the star formation rate can explain the paucity of these galaxies in the CNOC sample.

Kodama & Bower (2000) test these possibilities using colour magnitude diagrams to determine statistical star formation histories. They find that a model where the rate at which galaxies are accreted to the cluster declines smoothly, combined with the decline of star formation of galaxies in the field, can explain the BO effect. The observed colour distribution can not be explained by models with an abrupt truncation of the star formation, but if it declines over a timescale of 1 Gyr after accretion the results are consistent with observations. Balogh et al. (2000) come to similar conclusions considering the origin of gradients of star formation and colours within the cluster. They use cluster mass accretion rates from numerical simulations and assume an initial star formation of the galaxy entering the cluster typical of a field galaxy (supported by accretion of gas from the surroundings). The effect of the cluster is to remove the reservoir of gas causing a gradual decline in the star formation as the galaxy consumes the rest of it gas. This process has been also called "strangulation". The models presented by Balogh et al. (2000) allow for timescales from 1 to 3 Gyr to "truncate" star formation and show that an abrupt truncation leads to an overabundance of post-starburst galaxies. The radial gradients of galaxy properties within the cluster therefore arise from gradients in accretion times; galaxies in the cores are redder and have lower star formation rates because they were accreted earlier than galaxies in the outer parts of the cluster. On the other hand the authors also point out that their analysis cannot distinguish between other processes that can operate once the galaxy has been accreted into the cluster, such as tides, harassment or ram pressure stripping, because they operate in similar timescales.

Models based in a hierarchical picture, combining semi-analytic models for galaxy formation and N-body simulations of cluster formation (Diaferio et al. 2000), can produce a successful picture for the evolution of star formation rates and also for the morphological gradients in clusters. This model assumes that galaxy morphology is determined only by its merging history, where the merger of galaxies of similar mass produces a bulge and therefore the fraction of bulge-dominated galaxies is higher in the cluster core.

Another piece of evidence consistent with the model where late-type galaxies are infalling into the cluster, is the fact that they have larger velocity dispersion than early-types. This has been observed in distant clusters (Carlberg et al. 1997) and in Coma (Andreon 1996, Colless and Dunn 1996). The velocity dispersion of star-forming (emission line) galaxies is also larger than for quiescent ones. These observations are interpreted as a different formation process for the different types of galaxies, suggesting (Adami et al. 1998 and 2000) that the cluster population evolves through dynamical friction and infall, where star forming, late-type galaxies are currently infalling into the cluster.

In summary, there is not a single scenario to explain the spectroscopic, photometric and morphological transformations of the galaxy populations in rich clusters and probably it is a combination of some or all of them which causes the whole evolutionary picture.

1.6 Motivation and Aims of this Thesis

As seen in the previous review, a big effort has been made to explain galaxy evolution in clusters, but up to now the observations have been directed toward the richest (most L_X luminous) clusters. However, in order to be able to distinguish between the different mechanisms that can cause the transformation of the cluster population, we need further studies of systems in low and intermediate density environments.

The effectiveness of the different mechanisms suggested as being responsible for the transformation of the cluster population depends on the local environment. Ram pressure stripping is only effective in very high gas density regions, where the intra-cluster medium is dense enough to remove the gas from the disc. Mergers on the other hand are more effective in low density regions because the relative velocities of the galaxies are smaller.

With the aim of distinguishing between the different candidate mechanisms we have selected nine poor clusters at an intermediate redshift and, we will try to answer the following topics: does the blue fraction of galaxies evolve with time in poor clusters as it does it in rich clusters? do the morphological fractions of galaxies and the density-morphology relation evolve in a similar way to that found in rich clusters? how are colours and morphological types related in these low density environments? are the gradients of galaxy properties within poor clusters consistent with the evolution of galaxies in the field?

So how do we intend to study these topics? This thesis is part of a larger project, and does not attempt to answer all of the questions addressed above. In this work we will concentrate on four of the nine clusters of the sample, and specifically we will study the blue fraction of galaxies and compare it with the existing results for rich clusters.

In Chapter 2 we describe the selection of our sample of clusters and the data set we have obtained. This includes ground base photometry, multi-slit spectroscopy and HST images. We will explain how the photometry data has been reduced and calibrated in order to obtain magnitudes and colours for the galaxies in the clusters. The analysis of the spectroscopic data was not done as part of this thesis, but we

will briefly describe it and use the results. In Chapter 3 we will explain how we constructed the Colour Magnitude Diagrams for our subsample of four clusters and will calculate the blue fraction of galaxies following the original definition of Butcher and Oemler.

In Chapter 4 we will show the mosaic HST images for our clusters. We will also describe the morphological analysis performed on these images and will show some preliminary results regarding the morphological fractions of the galaxy population in these clusters.

The comparison of our results for the blue fractions with existing results for rich clusters is done in Chapter 5. In view of our results for the morphology and the blue fraction in our poor clusters, we will discuss in this chapter how they can help us to distinguish between the different mechanisms proposed to be transforming the galaxy population in clusters.

Finally in Chapter 6 we will summarize our analysis and conclusions and will outline the future prospects for the project.

Chapter 2

The Poor Cluster Sample

In order to study the topics outlined in the previous section regarding the evolution of galaxies in poor clusters, we have selected a sample of nine poor clusters at intermediate redshift. In this chapter we will describe how the sample was selected, and the data set we have obtained. In summary, this consists of ground-based photometry in several bands, from which we can obtain magnitudes and colours, and hence calculate the blue fraction of galaxies. We also have multi-object spectroscopy which will allow us to determine cluster membership (ie: correct for foreground/background contamination) and study the star formation history. In order to have an accurate morphological classification our sample of clusters has been observed with HST.

The layout of the chapter is as follows: Section 2.1 describes the sample of clusters and how it was selected. In Section 2.2 we describe the ground based imaging data: we give a summary of the observations, outline the reduction method and explain how the photometry was performed and calibrated. Section 2.3 gives a description of the results from the spectroscopic data.

2.1 The Sample

Our sample consists of 9 poor clusters, X-ray selected from the Vikhlinin et al. (1998) catalogue to have an X-ray luminosity $\sim 10^{43} erg\ s^{-1}$, one order of magnitude less than typical rich clusters, and redshift in the range $z \sim 0.2$ to 0.3. In order to understand how our sample of clusters was selected, we will first give a brief summary of the source catalogue.

2.1.1 The Vikhlinin Catalogue

The Vikhlinin catalogue (Vikhlinin et al. 1998) is one of the largest X-ray selected samples. It consists of 203 clusters of galaxies detected as being extended X-ray sources after analysing 647 ROSAT PSPC pointings. The ROSAT (the ROentgen SATellit) Position Sensitive Proportional Counter (PSPC) has a field of view with a diameter of 2°. In the Vikhlinin et al. (1998) catalogue, only pointings at high galactic latitudes were used, covering a solid angle of 158 deg^2. 91% of the resolved X-ray sources in the sample are optically confirmed as being clusters of galaxies, and are therefore included in the final cluster catalogue. Out of the 203 clusters detected, 73 have spectroscopic redshifts, while photometric redshifts are given for the rest. The cluster redshifts are in the range z=0.01 to $z = 0.7$. The catalogue also gives the X-ray flux and core radii for the clusters. The X-ray luminosities vary from 10^{42} to $5 \times 10^{44} erg\ s^{-1}$, corresponding to poor groups and rich clusters respectively.

2.1.2 Our Sample

Our target list was drawn from the Vikhlinin catalogue by applying the following criteria . We restricted our selection to those clusters with spectroscopically-confirmed redshifts within $0.2 < z < 0.3$. Applying the redshift limits to the Vikhlinin et al. (1998) catalogue and restricting the sample to those clusters observable from the Northern Hemisphere, we arrive at a sample of 28 clusters. From these we select those with $L_X < 0.8 \times 10^{44} erg\ s^{-1}$. This contrasts to luminosities $L_X > 2 - 20 \times 10^{44} erg\ s^{-1}$ for the X-ray selected clusters studied by HST so far, or roughly 1 to 2 orders of magnitude less luminous. Applying this upper flux cut-off to our subsample then leaves us with 9 clusters. Table 2.1 shows the position, luminosity and redshift of each of the 9 clusters of our sample. The redshifts given in table 2.1 are calculated after the analysis of our spectroscopic data, except for V191 and V192 for which this data was not yet available and the redshift from the Vikhlinin catalogue is given instead. The Vikhlinin values for the redshifts are less accurate than ours because they are based on measurements on only 2-3 galaxies per cluster.

ID	RA(2000)	DEC(2000)	$L_x(10^{43} erg\ s^{-1})$	z
V48, Cl0818	8 18 58	56 54 34	1.64	0.2478
V49, Cl0819	8 19 23	70 54 48	1.38	0.2296
V57, Cl0841	8 41 43	70 46 53	1.34	0.2396
V62, Cl0849	8 49 11	37 31 25	2.11	0.2347
V131, Cl1309	13 9 56	32 22 31	2.16	0.2938
V165, Cl1444	14 44 8	63 44 58	4.27	0.2968
V181, Cl1633	16 33 40	57 14 37	0.53	0.2406
V191, Cl1703	17 1 46	64 21 15	0.43	0.220*
V192, Cl1702	17 2 13	64 20 0	0.81	0.224*

Table 2.1: Our sample of clusters. * corresponds to redshifts from the Vikhlinin et al. 1988 catalogue.

2.2 Ground-Based Data: Reduction and photometric Calibration

2.2.1 Ground-Based Observations

Our ground-based imaging data comes from different observatories: Calar Alto, (where CAFOS in the 2.2m telescope and MOSCA (imaging mode) in the 3.5m telescope were used), the INT and the 200-inch Hale Telescope at Palomar Observatory.

Table 2.2 is a summary of the ground based imaging data available for each cluster. Here Ca2.2 and Ca3.5 refers to the 2.2m and 3.5m telescopes at Calar Alto Observatory respectively. P200 refers to data from Palomar. For the Ca3.5 run, n1 to n4 corresponds to the 4 different nights of observation for this run (see Section 2.2.1). In the table, each cluster is denoted by two names: the Vikhlinin et al. (1998) name and the one following the standard coordinate notation, we will use the latter to designate our clusters.

In this thesis I will concentrate on four of the nine clusters of the sample, these are clusters Cl0819, Cl0841, Cl0849 and Cl1633 (which are indicated in bold font in table 2.2). For Cl0819, Cl0841 and Cl1633 the R band data from the 2.2m telescope

at Calar Alto and the B band data from the 3.5m telescope is used. For Cl0849 the R data from Calar Alto had poor seeing (2.5") and the Palomar R image is used instead. In the following sections a description of these observations is given.

Table 2.2: Ground Based Imaging Data

Name	I	R	B	V
V48, Cl0818	Ca2.2 1.2ks	P200 0.5ks	P200 0.6ks	-
V49, Cl0819	Ca2.2 1.8ks	Ca2.2 0.6ks	Ca2.2 0.3ks	-
		P200 0.5ks	P200 0.6ks	
			Ca3.5-n1 1.2ks	
V57, Cl0841	Ca2.2 1.8ks	Ca2.2 0.6ks	Ca2.2 0.3ks	-
		P200 0.5ks	P200 0.6ks	
			Ca3.5-n1 1.2ks	
V62, Cl0849	Ca2.2 1.2ks	Ca2.2 0.6ks	Ca2.2 0.3ks	-
		P200 0.5ks	P200 0.6ks	
			Ca3.5-n2 1.2ks	
			Ca3.5-n3 0.6ks	
			Ca3.5-n3 0.3ks	
V131, Cl1309	Ca2.2 0.6ks	Ca2.2 0.6ks	Ca3.5-n4 5.4ks	Ca2.2 0.3ks
	INT 1.2ks	INT 2.4ks		INT 1.8ks
V165, Cl1444	Ca2.2 0.3ks	Ca2.2 0.3ks	Ca3.5-n4 5.4ks	Ca2.2 0.3ks
	INT 0.7ks	INT 2.4ks		INT 1.1ks
V181, Cl1633	Ca2.2 0.3ks	Ca2.2 0.6ks	Ca2.2 0.3ks	Ca2.2 0.3ks
	INT 1.2ks	INT 2.4ks	Ca3.5-n2 1.2ks	INT 1.8ks
			Ca3.5-n3 1.2ks	
V191, Cl1703	INT 0.9ks	Ca2.2 0.3ks	Ca2.2 0.3ks	Ca2.2 0.3ks
		INT 2.4ks	INT 2.4ks	
V192, Cl1702	INT 0.9ks	Ca2.2 0.3ks	Ca2.2 0.3ks	Ca2.2 0.3ks
		INT 2.4ks	INT 2.4ks	

Calar Alto 2.2m

These observations were performed by R. G. Bower during the night of the 28th of March of 1999 at the German-Spanish Astronomical Center at Calar Alto, using

the 2.2m telescope. The focal reducer CAFOS was used in its imaging mode. This instrument reduces the original plate scale of $85.4\mu m/arcsec$ to $45.2\mu m/arcsec$. The SITe-1d 2048 $\times$ 2048 CCD chip was used, which provides the widest field of view (16' diameter) and the best performance of the available detectors to be used with CAFOS (readout noise=5.06 e^-, gain=2.3 e^-/ADU). The scale of the chip is $24\mu m$ per pixel, which gives a scale of 0.53 $arcsec/pixel$.

Clusters Cl0819, Cl0841, Cl0849 were observed in Photometric conditions in B, R and I bands. Cl1633 was also observed in V. The V and B frames are, in all cases, not deep enough to provide useful information due to contamination from moon light. The I data suffers from fringing. Therefore only the R band from this observation run will be used. We have one R exposure of 600 seconds for each of the four clusters. The seeing was variable throughout the night, being 1.9" during the R exposure for Cl0819 and Cl0841, 1.6" for Cl1633 and rising up to 2.5" for Cl0849. As we will see later, fortunately we have another R image from this cluster taken at Palomar in better seeing conditions.

For calibration purposes standard stars from the Landdolt catalogue were observed also in B, V, R and I bands at intervals during the night. Four fields were observed, some of them containing several standard stars.

Calar Alto 3.5m

The shallowness of the B band data from the observation run at the 2.2m telescope at Calar Alto is the reason for which new data in B was taken at Calar Alto, this time at the 3.5m telescope and using MOSCA. The initial intention of this run was to obtain multi-object spectoscropy for our sample of clusters, but the time allocated allowed for some B imaging data to be taken. The whole run consisted of four nights of observation, from the 3^{rd} to the 6^{th} of March 2000. These observations were performed by B. L. Ziegler.

MOSCA is a focal reducer installed at the focus of the 3.5m telescope, which allows to perform both multi-slit spectroscopy and direct imaging. It provides a field of view of 11' and a scale of $169.7\mu m/arcsec$. The detector is a 2048 $\times$ 4096 pixels CCD of 15 micron pixels, which gives a scale of 0.3208 $arcsec/pixel$. The readout noise is 4.4 e^- and the gain 1.1 e^-/ADU.

Clusters Cl0819 and Cl0841 were observed during the first night under good conditions, with seeings 1.1" and 1.5" respectively during the 20 minutes of exposure for each cluster. Cl0849 and Cl1633 were observed during the second night, but the seeing was high (up to 3.8") so new images of these clusters were taken during the third night. For Cl0849 we have a 10 minutes exposure with 1.4" seeing and a 5 minutes exposure with 1" seeing. One 20 minutes image with 1.4" seeing is available for Cl1633.

Since conditions were not photometric, no standard star observations were made.

Palomar

This observation run was carried out by I. R. Smail during the nights of November 26^{th} and 27^{th} 1998, using the COSMIC imaging spectrograph on the 5-m Hale telescope at Palomar. COSMIC is a re-imaging grism spectrograph, which can also be used as a direct imaging camera with a 9.75 arcmin square field of view. The detector is a thin 2048 $\times$ 2048 TEK CCD with a scale of 0.286 *arcsec/pixel*. Individual R and B exposures of 250-300secs were taken with in-field dithering (on a grid with 30" spacing), producing frames of total exposure times of 500 and 600 seconds in R and B respectively. The seeing was relatively high and the night was non-photometric, so no calibration is available. Nevertheless, because as mentioned above the R image for Cl0849 from the Ca2.2 run has a seeing of 2.5", we will instead use the Palomar R image for this cluster, which has a seeing of 1.7".

2.2.2 Reduction

Here I will outline the steps followed to reduce the B and R images for Cl0819, Cl0841, Cl0849 and Cl1633.

These ground based images were reduced using the task *ccdproc* in IRAF, following the standard procedure and taking into account the different characteristics of each telescope and instrument utilised. First a summary of the standard reduction procedure in IRAF will be given, followed by a description considering the characteristics of each data set.

- The bias output signal (or pedestal level) is removed using the "overscan"

region for every frame. This has to be done individually since this signal can vary with temperature or telescope position. The data is averaged over the columns in this region, fitted as a function of the line-number and subtracted from each column in the frame.

• In order to correct for column to column variations in the bias level , frames obtained with a zero integration time are used. These are called bias (or "zero") frames and they are combined using the task *zerocombine* in IRAF. The resulting frame is then subtracted from all the other frames.

• In order to remove pixel to pixel gain variations of the chips and any large scale spatial variation along the detector, the data needs to be divided by the "flatfield". With this aim "dome flats", exposures of an illuminated white patch on the dome, are obtained for every filter. Sometimes the response of the CCD can vary between a dome flat and a sky exposure, in this case using "sky flats" (exposures of bright twilight sky) can usually solve the problem. A flat-field is created by combining the dome flats or sky flats using the task *flatcombine*. Finally the data frames are flattened after dividing by the combined flat.

After applying the procedure outlined above, the instrumental signal will be removed from our images.

R data from Calar Alto 2.2m

The bias pedestal level was removed using the overscan region for every frame as described above. 16 bias frames were combined and the result was subtracted from all the other frames to remove variations in the bias level. We have 4 domeflats and 3 sky flats to be used for the R data for this night of observation.

A flat field was created by median combining the domeflats using the task *flatcombine*. Dividing the images by the combined domeflat for the R data removed the pixel to pixel variation of the chips but after flatfielding, the images showed a gradient in the sky level up to 4%. For this reason a flatfield was created by median combining all the science frames in R band for this night of observation. Dividing the images by this flatfield removed the pixel to pixel variation and also the gradient in the sky level, which is reduced to 1% or 2%. This can be seen in the bottom panel of figure 2.1 which shows the number counts along a line of the chip.

B data from Calar Alto 3.5m

The overscan region was used as previously explained to remove the bias output signal. For this run 9 "zero frames" were combined in order to remove the column variations of the bias level.

As indicated in section 2.2.1 this B data was taken over 4 nights, we have 5 domeflats and 7 sky flats for the first night of observation, while there are only 3 sky flats for the second night and none was taken in the third and forth nights. The seeing in the second night was very high (up to 3.8") so the data for this night is not useful. Therefore only the data from the first, third and fourth nights is of use. Since there are no sky flats available for the third and fourth nights, the dome flats will be used to flatfield. For the first night we decided to use the dome flats as well (if we compare the dome and sky flats for this night, dividing one by the other, we see that they do not differ significantly).

By dividing the B band images by the combined domeflat, we removed the pixel to pixel variations. Using the domeflats to flatfield did also succeed in this case to remove possible gradients in the sky level. (See top panel of figure 2.1).

R data from Palomar

The frames were reduced following the standard procedure in IRAF. The data was flatfielded using twilight flat fields, which were aligned and coadded using a cosmic ray rejection algorithm. The flatfielding was successful in removing large structure spatial variations and the image we will use (Cl0849) does not show any gradient in the sky level.

2.2.3 Image Transformations: Geometry and PSF.

We are going to perform and compare photometry of the same objects coming from different instruments: CAFOS at the 2.2m telescope (R band), MOSCA at the 3.5m telescope (B band) and Palomar (R band), so we first need to geometrically transform the images to a chosen reference system. Also, since the seeing varies in some cases between the R and the B frame of the same cluster, the PSF (Point Spread Function) must be matched between the two frames before doing aperture

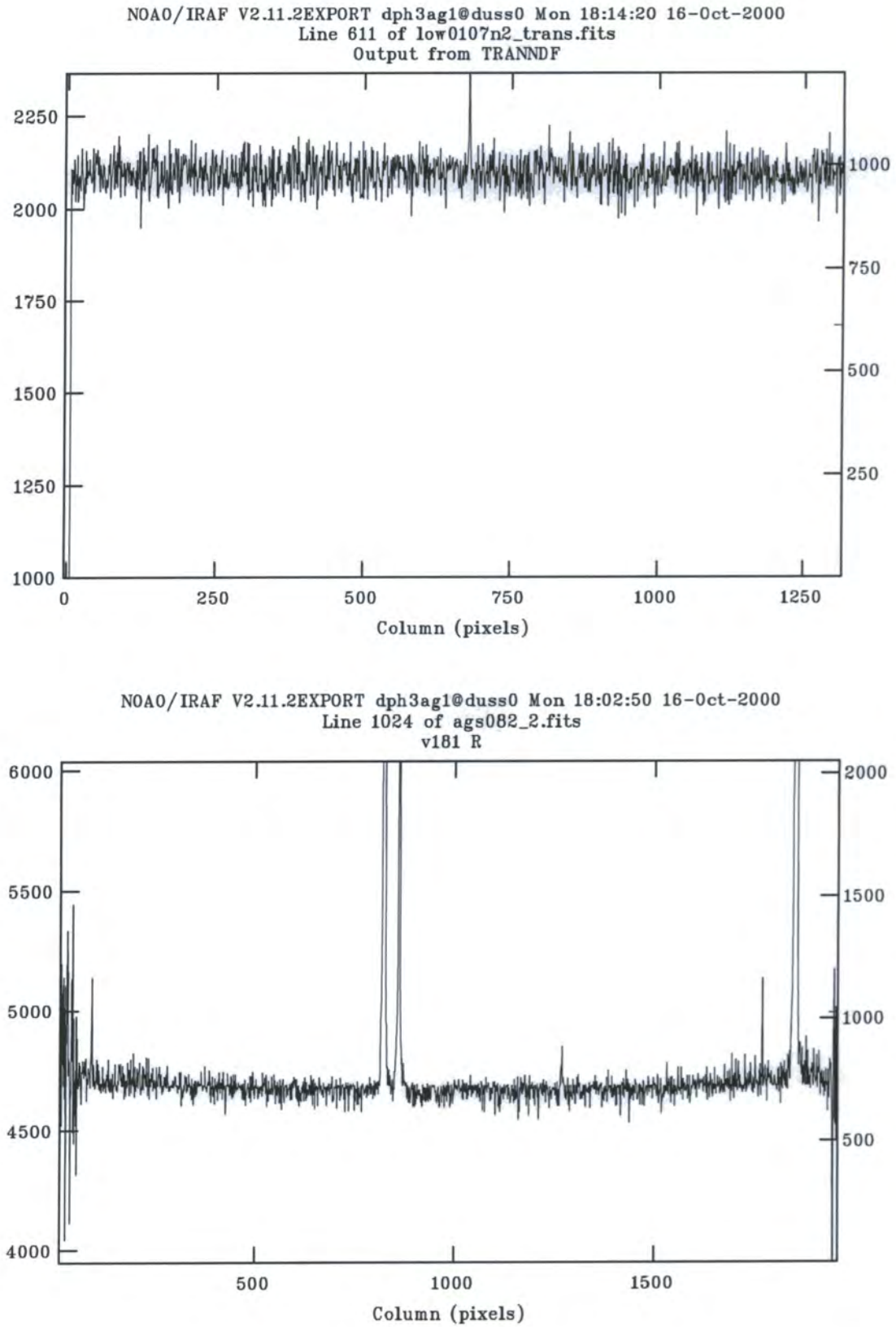

Figure 2.1: line plots for B (top panel) and R (bottom panel) frames after flatfielding

photometry. In this way we are able to use the same aperture to perform photometry in both the R and B frames of a cluster.

We use the task *geomap* in IRAF to calculate the geometry transformations between different instruments. In this way we computed the transformation required to map the Calar Alto B frames from the 3.5m telescope to the 2.2m telescope instrument geometry (ie the R frames). The fitting geometry used in *geomap* is *rxyscale*, which allows for x and y shifts, x and y magnifications, a rotation angle and axis flips. The results from *geomap* are given in the form of a set of six coefficients which defines the transformation between the reference and the input frames. This set of coefficients was used to transform the images using the packages CCDEDIT and TRANNDF in CCDPACK. The fit residuals of the computed geometry transformations are in all cases smaller than 0.4 pixels.

Since the geometry of the R frames from the 2.2m telescope was used as a reference, the R frame for Cl0849, coming from the Palomar observatory, was also transformed to this system. So finally we have transformed all of our clusters images to the same geometry, and hence each pair of R and B frames of a given cluster have the same coordinate system.

In order to match the PSF of the pair of R and B images for each cluster, the task *psfmatch* in IRAF was used. The objects used to calculate the convolution kernel were chosen to be isolated and were selected by inspecting radial profiles. In this way the PSF of the image with a higher resolution is broadened to match the corresponding poorer resolution image. This process had to be applied to the B frames of clusters Cl0819, Cl0849 and Cl0841. For Cl0819 the B frame had a seeing of 1.1" while the R data seeing was 1.9", so the first one had to be broadened. For cluster Cl0849 the 1" seeing of the B band image had to be matched to the 1.7" corresponding to the R image. The B image for Cl0841 had a seeing of 1.4" and was transformed to match the 1.8" of the R image.

For cluster Cl1633 the difference between the seeing of the R and B frames is smaller and the PSF was not transformed. The R image has a seeing of 1.5" while the B image seeing is 1.6", but this difference is of the same order as the accuracy obtained when matching two different seeings, hence not transforming the B image

for this cluster is justified.

2.2.4 Photometry

Having transformed the frames to the same geometrical system, and having transformed the PSF's to correct for differences in the seeings, we are ready to perform aperture photometry on our images. Photometry was done to objects detected by running *SExtractor* (*Source Extractor*), a program which was developed to analyse moderately crowded astronomical images. *SExtractor* selects objects by detecting groups of connected pixels whose values are greater than a given threshold above the background. (see *SEextractor v2.0 user's guide* by E. Bertin). *SExtractor* gives other useful information: several flags indicating possible problems like the proximity of a neighbour, truncation or saturation of the object and the *stellarity* (or *"star-class"*) of the detected objects, which will be used in order to do the galaxy/star separation. This parameter ranges from 0 to 1, being close to 1 for stars and close to 0 for extended objects.

The coordinates of objects given in the *SExtractor* catalogue are used as an input in the task *phot* in IRAF to perform aperture photometry. The specific characteristics of the data, such as FWHM of the PSF, CCD readout noise, CCD gain, exposure time and airmass are included here in the parameter *datapars* (see table 2.3 for an example of a *datapars* file) . The aperture radius is set in *photpars* and the sky fitting parameters in *fitskyp*. With this information *phot* calculates the sky value for each object and computes the corresponding magnitude.

In this way, instrumental magnitudes for the R and B band data were obtained. Since the frames had already been geometrically transformed and the PSF had been matched as described in the previous section, the same aperture radius was used for the photometry on the B and R frames of a cluster. For all the four clusters Cl0819, Cl0841, Cl0849 and Cl1633 a radius of 5 pixels (2.65") was chosen, this makes an aperture diameter of 5.3" and compares to values of the fwhm of 1.9", 1.8", 1.7" and 1.6" respectively.

In choosing the aperture diameter one has to take into account that small apertures will contain a small fraction of the light, but on the other hand large apertures

will contain too much sky noise, and therefore will reduce the signal to noise ratio (SNR). Also, in our case, it has to be considered that large aperture radii will contain light from neighbours. Our choice of an aperture radius of 5 pixels (2.65") is a compromise between both extremes. In order to asses how much light is lost we can compare the magnitudes that we would obtain if using a larger radius. This has to be done on objects that do not have a near neighbour, so the magnitude measured with the larger aperture is not contaminated by light from the near object. Hence we selected isolated galaxies and examined the difference obtained between using our radius and a radius 1" larger. However, choosing this larger radius leads to contributions from neighbours in most cases, so we decided to use the 5 pixel aperture radius. It also has to be noticed that the different radius size will mainly affect the brighter galaxies (where we found differences of around 0.1 magnitudes). But this does not have a very significant effect on the fainter galaxies for which, in any case, the errors are larger than this effect. This will therefore not affect our results regarding the blue fraction because, as we will see in the calculation of the blue fractions (Section 3.3), the blue galaxies are at the faint end of the CMD.

Table 2.3: Example of *datapars* file for the Calar Alto 2.2m data.

PACKAGE = apphot	
TASK = datapars	
(scale =	1.) Image scale in units per pixel
(fwhmpsf=	3.5) FWHM of the PSF in scale units
(noise =	poisson) Noise model
(ccdread=	CCDRON) CCD readout noise image header keyword
(gain =	CCDSENS) CCD gain image header keyword
(readnoi=	5.06) CCD readout noise in electrons
(epadu =	2.3) Gain in electrons per count
(exposur=	EXPTIME) Exposure time image header keyword
(airmass=	AIRMASS) Airmass image header keyword
(itime =	600) Exposure time
(xairmas=	1.231) Airmass

2.2.5 Calibration

Several problems arose when trying to calibrate the data. Firstly, as it is indicated in section 2.2.1, standard stars where not observed during all the nights, or were not

observed in all bands. Also, for some of the nights when calibration standards were observed, the data is not useful due to saturation. Standard stars were observed during the run at the 2.2m telescope at Calar Alto, but there are no calibration standards available for the observations at Palomar and the 3.5m telescope at Calar Alto.

Therefore it will be possible to calibrate only the data from the 2.2m Calar Alto run by using standard stars. The other data sets will be calibrated by other means as we will see next.

Calar Alto 2.2m R data

We have B, R and V frames for standard stars for this night of observation. Although only the R band data for the clusters from this run is going to be used, we will use all the three bands data for the standard stars, which allow us to take into account colour terms in the calibration. Four standard fields from the Landolt 1992 catalogue were observed in the three bands, each containing several standard stars. These fields are PG1633+099, PG1323+086, PG1528+062, PG1047+003 and details about the observation are given in table 2.4. The frames in each band were reduced following the same procedure as for the R band data for the clusters (see section 2.2.2). Since only a small section of the CCD was used for the standard star frames, there were no large spatial variations along the image and using the combined domeflat gave a successful result. This does not represent a significant difference from the flatfielding applied to the cluster images: the combined domeflat and the flatfield used for the cluster frames were divided, and the result in the area of the chip used for the standard stars is only an offset in the sky level. Since *ccdproc* normalizes the flatfield when dividing the frames by it, the procedure is therefore consistent.

Photometry was performed individually for each standard star using *phot* in its interactive mode with an aperture radius of 7.8".

The transformation equations were solved using the task *fitparams* in IRAF. *Fitparams* uses an internal standard star catalogue (Landolt catalogue in this case) and an input catalogue with the instrumental magnitudes and airmasses of the observation to solve the transformation equations.

Having B, R and V images the transformation equations in the configuration file used by *fitparams* are the following:

$$BFIT : mB = (BV + V) + b1 + b2 \times XB + b3 \times BV + b4 \times BV \times XB$$

$$VFIT : mV = V + v1 + v2 \times XV + v3 \times BV + v4 \times BV \times XV$$

$$RFIT : mR = (V - VR) + r1 + r2 \times XR + r3 \times VR + r4 \times VR \times XR$$

Where mB, mV and mR are the instrumental magnitudes in each filter; B, V and B are magnitudes from the Landolt catalogue and BV, VR stand for the colours (B-V) and (V-R). The airmasses in each filter are denoted by XB, XV and XR. We set parameters $b4$, $v4$ and $r4$ equal to zero (note that this is a second order term).

Although four standard star fields from the Landolt catalogue were observed, only three of them (PG1633+099, PG1528+062, PG1047+003) were used to solve the transformation equations. The reason for this is that one of the fields (PG1323-086) has an airmass of 3, as it can be seen in table 2.4.

The resulting fit for the R band given by *fitparams* is :

$r1 = 1.7146 \pm 0.0630$

$r2 = 0.1753 \pm 0.0465$

$r3 = 0.0630 \pm 0.0261$

And the fit has a standard deviation of 0.0176. Figure 2.2 shows the residuals of the fit versus the "function" (ie the instrumental magnitude).

Parameter r1 is the *zero point*, r2 is the *extinction coefficient* and r3 the *colour term*. With these three parameters the equation to be used in order to calibrate the instrumental magnitudes in R for our clusters is :

$R = r - Kr \times a - ZPr - r3 \times (V - R)$, with:

$ZPr = 1.71 \pm 0.06$

$Kr = 0.17 \pm 0.05$

Since we do not have V frames for the clusters, we do not have a V-R measured instrumental colour. Instead, we can use a typical V-R value for a galaxy at a similar redshift. Fukugita et al. (1995) give a value of $V - R_J = 0.93$ for an elliptical galaxy at a redshift of 0.2. With this value the contribution of the colour term to the R calibration is $r3 \times (V - R) = 0.06$ magnitudes.

So finally, the calibration equation to apply to the instrumental R magnitudes from the Calar Alto 2.2m run is:

$$R = r - 0.17 \times a - 1.71 - 0.06$$

where the value for the airmass is 1.231, 1.283 and 1.090 for clusters Cl0819, Cl0841 and Cl1633 respectively.

Table 2.4: Standard Star Fields

ID	filter	Airmass
PG1633+099B/+099C/+099D	R1	1.239
	R2	1.127
	V1	1.233
	V2	1.127
	B1	1.228
	B2	1.127
PG1323-086B	R1	2.939
	R2	2.939
	V1	2.991
	V2	2.991
	B1	3.042
	B2	3.042
PG1528+062/+062A	R1	1.312
	R2	1.312
	V1	1.329
	V2	1.337
	B1	1.352
	B2	1.352
PG1047+003A/+003	R1	1.296
	R2	1.482

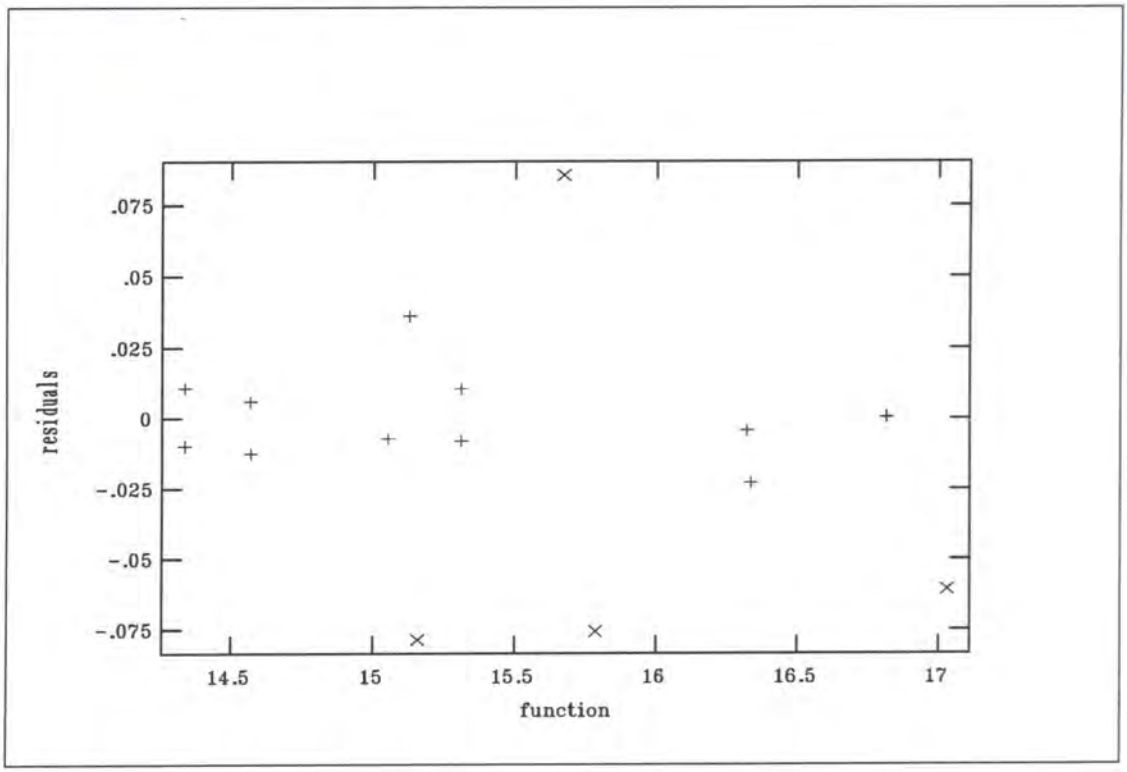

Figure 2.2: The residuals as a function of the fit from *fitparams*. Crosses are points which are rejected in the fit.

Palomar R data

As mentioned before, the night of observation for this run was non-photometric. Nevertheless we can calibrate this R band data by comparing it with the R data from the Calar Alto 2.2m run, for which calibration is available. The reason for which the Palomar R image of Cl0849 is used instead of the one from Calar Alto 2.2m, is that the latter has a very high seeing. But it can still be used to calibrate the Palomar image. We first obtain magnitudes for isolated compact objects (isolated stars) in the Calar Alto image and calibrate these magnitudes using the calibration equation in the same way as discussed in the previous section. Instrumental magnitudes for these same objects are taken in the Palomar image and the difference between these instrumental magnitudes and the calibrated magnitudes from the Calar Alto image are calculated. We can use the median of the differences to calibrate the Palomar data for Cl0849 by adding it to the Palomar instrumental magnitudes.

Following this procedure isolated compact objects were selected, giving a median value for the difference between the calibrated magnitude from Calar Alto and the

instrumental maginute from Palomar of 0.05 magnitudes, with a standard deviation of 0.019 magnitudes. Therefore the R Palomar data can be calibrated by applying the following equation (where capital R refers to calibrated magnitudes and small r to instrumental magnitudes):

$R_{Pal} = r_{Pal} + meandiff$, where meandiff is:

$meandiff = mean\ of\ (R_{CalarA} - r_{Pal}) = 0.05$

Calar Alto 3.5 B data

Since no standard stars were observed during this run an alternative calibration method has to be applied. We can use predictions from stellar population models at the different cluster redshifts to calibrate the B-R colour by assuming a slope and zero point for the red sequence of galaxies. Since doing this requires having constructed the Colour-Magnitude diagrams and knowing which galaxies are members of the cluster, we will explain the method after describing the spectroscopic data.

2.3 Spectroscopy

Multi-object spectroscopy has been obtained using MOSCA at Calar Alto and LDSS2 on the WHT in La Palma. Three observation runs were done using MOSCA: the nights of the 11^{th} and 12^{th} of April 1999 (observer R. G. Bower), four nights from the 3^{rd} to the 7^{th} of February 2000 and the 30^{th} and 31^{st} of July 2000 (observer B. L. Ziegler). The LDSS2 run was carried from the 2^{nd} to the 5^{th} of March 2000 at the WHT (observers R. G. Bower and A. Gaztelu).

All the data has been reduced and redshifts and linewidhs have been measured. The data from LDSS2 is not of a very good quality mainly due to a high seeing during the observing run.

I reduced and analysed some spectra during the observations at the WHT to check on integrations times. However all the data has been re-reduced and analysed by Michael Balogh; I will briefly summarize our reduction method and procedure to obtain redshifts and velocity dispersions from the spectra.

2.3.1 Reduction and Analysis

The two dimensional spectra were median combined to remove cosmic rays, and the bias was subtracted from the combined image. The one dimensional spectra were extracted with standard IRAF packages. No flat field correction or flux calibration was applied. Wavelength calibration was done using a CuAr arc lamp spectrum; the r.m.s. dispersion in the wavelength solution is typically 0.5 Å.

Redshifts were measured by cross-correlating the spectra with a series of galaxy and stellar templates, using the IRAF task *fxcor*. Typical velocity uncertainties are about 75 km/s.

Cluster velocity dispersions are in the range 300 to 700 km/sec and were estimated in the following manner. First, an initial guess at the central redshift is made, and the mean and variance (σ^2) of the redshifts within $\Delta < 0.01$ of this guess is computed. These quantities are then recomputed, after rejecting galaxies more than 2σ away from the mean, to exclude outliers. The mean velocity uncertainty of the galaxies within this cut is also computed, and this is subtracted in quadrature from the variance to obtain the cluster velocity dispersion; this is then divided by

(1+z) to convert to the rest frame.

The redshift range to use for considering membership to the cluster is calculated from the velocity dispersions, taking those galaxies within 3σ as members.

Table 2.5: Summary of Spectroscopy

CLUSTER	z	V disp km/s	Spectra	Unique Redshifts	Members
Cl0818	0.2478	304	53	20	5
Cl0819	0.2296	343	39	36	21
Cl0841	0.2396	331	35	30	20
Cl0849	0.2347	663	70	41	28
Cl1309	0.2938	446	120	42	24
Cl1444	0.2968	531*	66	46	29
Cl1633	0.2406	621	58	46	18
Cl1701	0.220	392	48	41	16
Cl1702	0.242	1478*	48	41	17

2.3.2 Spectroscopic Results

Table 2.5 is a summary of the spectroscopic properties for each cluster. Here the redshift given in column 2 is the redshift derived from our spectroscopic data. Column 3 gives the velocity dispersions calculated as previously explained. Here * means that the velocity dispersion is not well defined (i.e. is not a Gaussian distribution). Note that this is not the case for any of the clusters that we are going to study here. The number of total spectra obtained for each cluster is given in column 4 and column 5 is the number of unique redshifts (ie not corresponding to the same object in different masks for one field). Column 6 gives the number of members.

Although table 2.5 summarises the properties for the entire sample, the following tables show in more detail the results from the spectroscopy for the four clusters

Cl0819, Cl0841, Cl0849 and Cl1633. The SNR, redshift, uncertainty (in *Km/sec*), and other comments such as the presence of absorption or emission lines are given for each slit of each mask for which spectra was obtained for these clusters. This information will be used later to make the CMD and calculate the blue fraction of galaxies in order to determine membership to the cluster and indicate objects with emission lines.

In the following tables we denote the different observation runs in this way: *Run 1*: MOSCA 1999; *Run 2*: MOSCA 2000; *Run 3*: LDSS2 2000.

-Cluster ***Cl0819*** was observed with three masks: two different ones during *run 2* and a third one during *run 3*. The two first ones are of a very good quality but no redshifts are obtained from the last one because of its bad quality. Tables 2.6 and 2.7 show the results for the two masks from the MOSCA run.

-Cluster ***Cl0841*** was also observed with three different masks: two in *run 2* and one in *run 3*. No redshifts are obtained from the last mask due to bad seeing. The spectra from the two masks from *run 2* are of good quality and the results are shown in tables 2.8 and 2.9.

-Cluster ***Cl0849*** was observed with one mask during *run 1* and two masks during *run 2*. The quality of the data from *run 1* is fairly poor; the first mask from *run 2* has a good quality and the quality of the second mask is marginal. Redshifts have been obtained from the three masks and tables 2.10, 2.11, and 2.12 show the results.

-Cluster ***Cl1633*** was observed with two masks in *run 1*, being both of good quality. The results can be seen in tables 2.13 and 2.14.

Table 2.6: CL0819 Mask 1

Aperture	SNR	Redshift	Uncertainty	Comments
1	5.7	0.4193	46 (Km s^{-1})	good, [OII], [OIII], Hβ
2	15.4	0.3141	90	good, [OII], H+K
3	1.5	-	-	(serendipitous) v. weak signal
4	11.7	0.22782	136	good, H+K
5	10.6	0.23123	120	good, H+K, [OII]
6	9.0	0.22956	104	good, H+K
7	4.2	0.49521	135	weak, H+K, [OII]
8	8.2	0.22770	98	good, H+K
9	11.7	0.23198	113	good, H+K
10	9.9	0.23191	145	good, H+K
11	9.2	0.22761	89	good, H+K
12	16.1	0.22999	129	good, H+K
13	12.6	0.23062	104	good, H+K
14	12.9	0.25165	98	good, H+K
15	9.7	0.23049	122	good, H+K
16	9.6	0.23029	134	good, H+K
17	10.6	0.22725	119	good, H+K
18	4.9	0.22864	147	various absorption lines
19	2.3	-	-	weak, bad sky subtraction
20	10.0	0.20656	61	[OII], Hα
21	9.8	0.30792	100	H+K
22	7.1	0.2301	52	[OII], [OIII], Hα
23	6.7	0.22797	132	H+K
24	14.7	0.1688	64	[OII], [OIII], Hα, rotation
25	8.4	0.19274	134	good, H+K
26	8.0	-	-	faint, bad sky subtraction

Table 2.7: CL0819 Mask 2

Aperture	SNR	Redshift	Uncertainty	Comments
1	13.6	0.13147	123 (Km s^{-1})	good, H+K, G band
2	11.5	0.31408	92	good, H+K
3	11.0	0.23044	139	good, H+K
4	8.8	0.23113	129	good, H+K
5	7.4	0.22861	133	good, H+K
6	7.1	0.2294	282	good, H+K
7	3.8	0.45279	122	weak
8	16.1	0.20676	93	good, H+K, [OII], Hα
9	14.5	0.25292	132	very good, H+K
10	8.0	0.33359	97	H+K, [OII]
11	9.4	0.23100	75	H+K
12	5.6	0.41916	48	H+K, [OII]
13	8.5	0.22874	68	[OII], Hα

Table 2.8: CL0841 Mask 1

Aperture	SNR	Redshift	Uncertainty	Comments
1	7.7	0.24237	87 (Km s^{-1})	H+K
2	4.7	0.33916	49	strong OII, OIII, Hβ, Hα emission
3	6.2	0.23817	91	H+K
4	9.5	0.32771	76	H+K
5	6.8	0.23628	87	[OII], Hα
6	8.9	0.24006	38	strong [OII], Hα emission with rotation
7	10.2	0.24005	69	H+K
8	8.8	0.23922	103	H+K
9	8.3	0.23732	88	H+K
10	12.2	0.23778	89	H+K
11	3.5	0.23839	146	maybe strong Hδ?
12	5.0	0.24270	152	OK
13	10.2	0.24000	83	H+K
14	6.6	0.54594	106	H+K, faint [OII]
15	5.3	0.24006	49	[OII], [OIII], Hα emission, rotation
16	4.8	-		no clear features
17	1.6	0.30007	58	weak [OII], [OIII]
18	6.9	0.24071	113	H+K
19	5.1	0.18081:	104	no clear features
20	3.5	0.45822	134	[OII], weak [OIII]
21	5.0	0.17777	126	[OII], Hα

Table 2.9: CL0841 Mask 2

Aperture	SNR	Redshift	Uncertainty	Comments
1	1.4	0.53143	62 (Km s^{-1})	[OII], [OIII], Hβ
2	2.4	0.54596	168	H+K, [OII](shares slit with 3)
3	0.5	0	-	M star (shares slit with 2)
4	1.9	-		very faint, no features (shares with 5, 6)
5	2.6	-		faint, no visible features (shares with 4, 6)
6	12.5	0.24018	74	bright, [OII],[OIII],Hα (shares with 4, 5)
7	4.6	0.24152	165	H+K
8	16.6	0.23973	86	H+K
9	6.9	0.24027	110	H+K
10	7.6	0.23960	110	H+K
11	7.9	0.23874	133	H+K (shares slit with 12)
12	1.6	0.	-	M star (shares slit with 11)
13	7.6	0.03879	89	Hα, [OIII] emission
14	5.2	0.23998	163	absorption lines?. Possible weak Hα

Table 2.10: CL0849 Run1 Mask 1

Aperture	SNR	Redshift	Uncertainty	Comments
1	7.2	0.23454	151 (Km s^{-1})	faint, poor sky subtraction
2	6.0	0.25316	280	no clear features
3	8.5	0.23544	91	faint, H+K
4	7.8	0.23414	81	very faint, [OII]
5	6.9	0.23415	215	absorption lines
6	6.0	0.23162:	563	Xcor solution dubious
7	5.5	0.23259	322	absorption
8	8.4	0.23173	113	H+K
9	8.7	0.23305	138	H+K
10	4.1	0.23767	231	possible absorption
11	6.7	0.23738	96	H+K
12	6.9	0.09943:	450	H+K? marginal Xcor result
13	8.4	0.22884	120	H+K
14	13.9	0.24017	92	H+K
15	11.6	0.23625	235	H+K
16	10.1	0.23881	125	H+K
17	8.2	0.23590	135	[OII]
18	5.7	0.23779	169	H+K
19	12.1	0.30557	80	bad sky, [OII]
20	3.7	0.	0.	M star
21	2.5	0.	0.	M star
22	-	-		right on bad column
23	3.8	0.22951	127	H+K
24	5.8	0.30757:	482	doubtful Xcor result
25	5.7	0.22035	205	weak H+K
26	7.9	0.23394	237	faint
27	8.2	0.37311:	494	bad, possible H+K
28	4.3	-		no Xcor solution
29	12.4	0.17777	136	possible absorption

Table 2.11: CL0849 Run2 Mask 1

Aperture	SNR	Redshift	Uncertainty	Comments
1	7.7	0.23558	13(Km s^{-1})	OK, H+K
2	6.2	0.23370	134	OK, H+K
3	8.9	0.23526	111	good, H+K
4	4.0	0.23326	208	faint
5	10.2	0.23307	150	good
6	5.2	0.23302	148	OK, H+K
7	4.2	0.23260	115	absorption
8	10.3	0.23215	94	good, H+K
9	5.2	0.23153	128	good, H+K
10	5.5	0.23395	87	good, H+K
11	5.4	0.23817	133	good, H+K
12	8.4	-		no features
13	7.4	0.22950	177	good, H+K
14	7.6	0.24075	91	good, H+K
15	6.7	0.23662	206	good, H+K
16	9.2	0.23831	157	good, H+K
17	6.7	0.23754	63	good, H+K
18	2.7	0.23824	214	OK, [OII]
19	3.8	0.30529	76	possible [OII]
20	2.0	0	-	M star
21	7.9	-		no recognizable features
22	9.4	0.31564:	251	possible H+K, no clear features
23	5.1	0.23493	140	absorption lines
24	3.4	-		faint, bad sky subtraction
25	4.6	-		OK, but no clear features
26	7.4	0.17796	109	OK, H+K?

Table 2.12: CL0849 Run2 Mask 2

Aperture	SNR	Redshift	Uncertainty	Comments
1	6.5	0.25307	94 (Km s^{-1})	OK, H+K, shares slit with 2
2	2.0	-		poor, shares slit with 1
3	13.1	-		no features
4	8.1	0.23413	130	H+K
5	3.6	0.23839	306	absorption lines
6	4.3	0.23915	148	H+K
7	3.6	0.23091	107	H+K, Hδ, G, shares slit with 8
8	8.1	0.21890	64	H+K, OII, shares slit with 7
9	3.1	0.23035	122	H+K
10	3.5	0.23146	212	faint, absorption lines
11	3.5	0.23511	73	H+K, [OII]
12	5.7	0.17910	128	absorption lines
13	2.1	0.	0.	M star
14	2.7	0.	0.	M star
15	3.7	0.23544	167	absorption lines?

Table 2.13: CL1633 Mask 1

Aperture	SNR	Redshift	Uncertainty	Comments
1	8.9	0.24077	79 (Km s^{-1})	H+K
2	4.5	0.24172	45	[OII], [OIII]
3	11.6	0.24498	26	[OII], [OIII], Hβ
4	9.5	0.31520	80	H+K
5	13.5	0.23884	96	H+K, [OII], Hδ
6	11.3	0.13339	90	H+K
7	3.4	0.24124	110	possible emission lines
8	2.9	0.35510	27	Hβ, [OIII]
9	5.8	0.23962	97	H+K
10	14.1	0.33063	96	H+K
11	6.9	0.23876	125	H+K
12	2.4	0.25010:	156	cannot confirm Xcor redshift
13	5.3	0.24037	171	absorption lines
14	8.8	0.24250	91	Hβ, H+K
15	11.5	0.24023	93	absorption lines
16	4.0	0.24297	112	absorption lines
17	14.7	0.13583	42	-
18	9.6	0.23701	93	H+K
19	5.0	0.34467	96	[OII]
20	8.7	0.23953	60	H+K
21	5.2	0.43856	63	[OII], [OIII], strong Hδ
22	4.0	0.27070	87	H+K, [OII]
23	3.0	0.54630	86	[OII]
24	5.7	0.13388	29	[OII], Hα
25	4.4	0.27106	45	[OII]
26	4.6	0.14954	35	[OII], Hα
27	3.3	-		no features
28	4.8	0.34334	24	[OII]
29	10.9	0.27131	63	[OII], H+K
30	11.6	0.24746	54	[OII], Hδ

Table 2.14: CL1633 Mask 2

Aperture	SNR	Redshift	Uncertainty	Comments
1	17.5	0.23980	174 (Km s^{-1})	H+K
2	5.0	0.31427	49	[OII]
3	10.7	0.24517	30	[OII], [OIII], (Hα), Hβ
4	13.0	0.31539	104	H+K
5	5.3	0.31489	278	possible absorption lines
6	16.5	0.13285	130	H+K
7	8.9	0.23770	117	H+K?
8	8.1	0.23709	89	(shares slit with 9) absorption
9	8.9	0.23870	133	(shares slit with 8) H+K?
10	19.5	0.33089	74	H+K
11	7.7	0.23985	147	no clear features
12	3.5	-		no solution
13	4.3	-		no features
14	4.6	0.23997	139	H+K?
15	11.3	0.23904	130	absorption
16	5.5	0.24166	188	absorption
17	2.2	-		no features
18	6.6	0.31576	237	(shares with 19, 20) absorption
19	2.2	0.03237:	101	(shares with 18, 20), Hα?
20	0.9	-		(shares slit sp18, sp19) nothing
21	12.1	-		M star
22	-	-		incorrectly extracted
23	5.1	-		no solution
24	4.5	0.27089:	209	weak Xcor result
25	4.6	0.26719	47	[OII], (Hβ)
26	8.3	0.27008	189	absorption
27	3.2	-		no features
28	1.7	0.27167	97	[OII]

With the results shown above from the spectroscopy we can make redshift histograms for the four clusters. Figure 2.3 has a large range in z and shows how the clusters are obvious structures in redshift space, here we can also see other foreground or background structures. The histograms are zoomed in figure 2.4, with a narrower range of z around the median redshift.

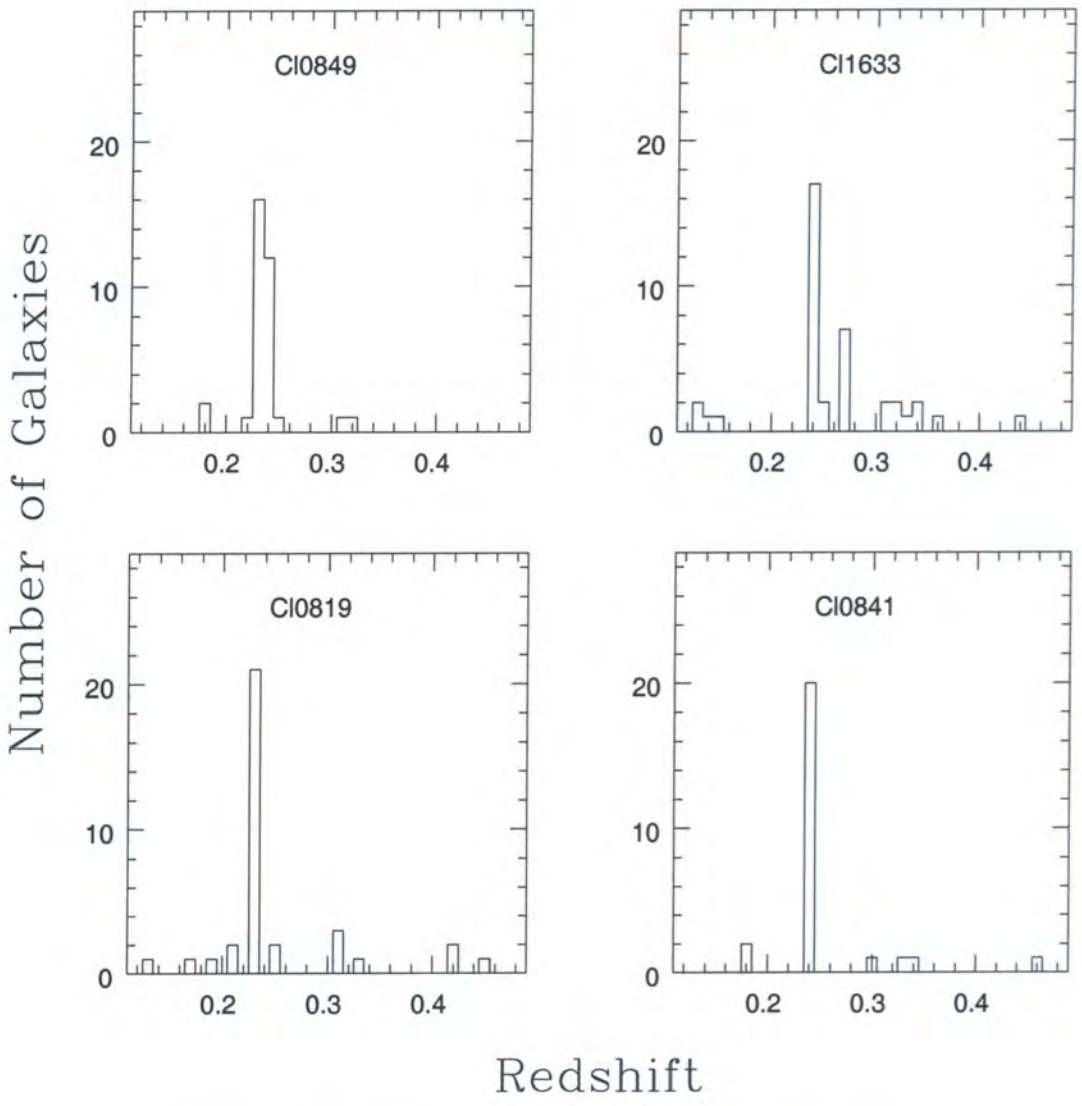

Figure 2.3: Redshift histograms with a large range of z.

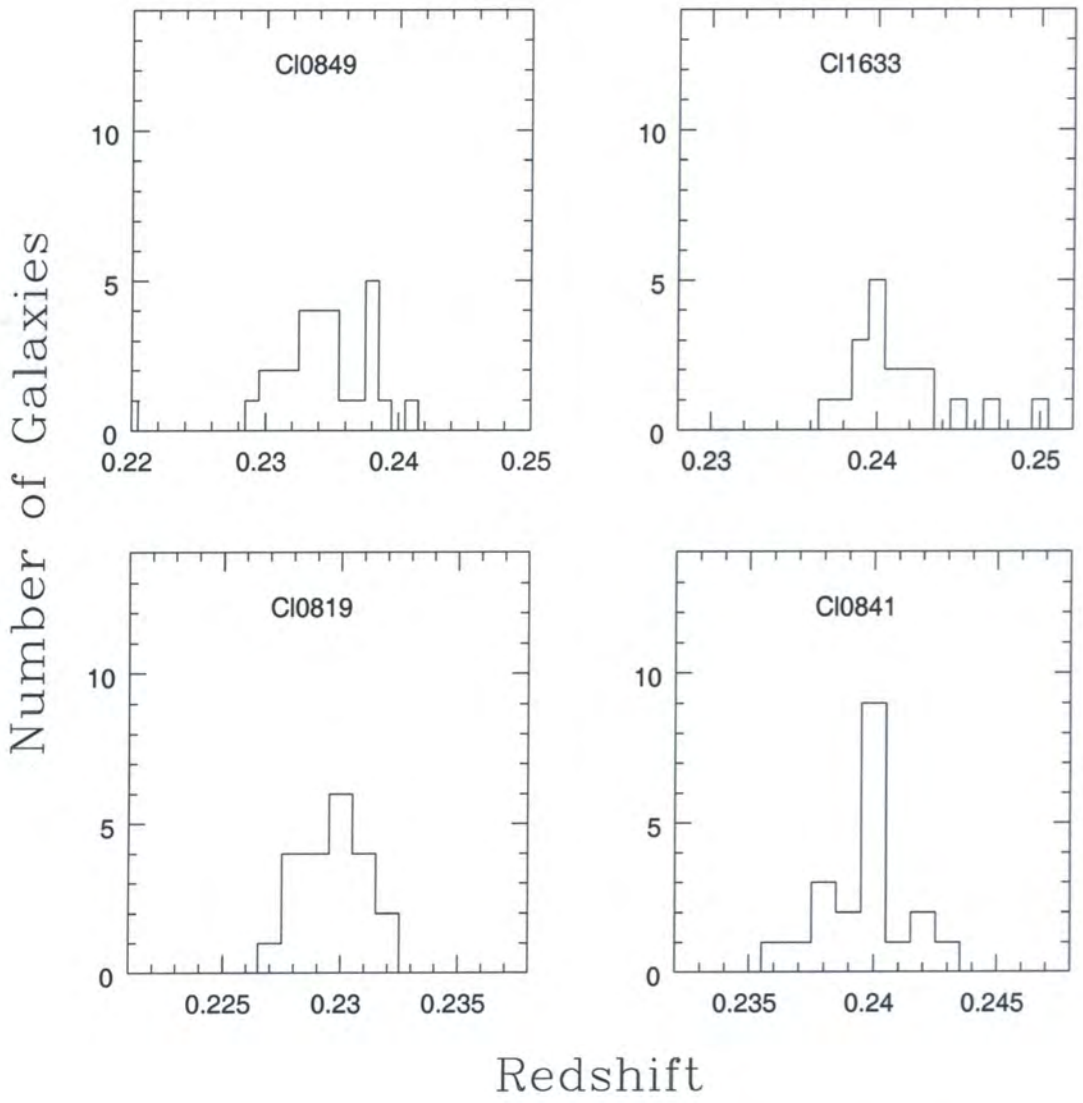

Figure 2.4: Redshift histograms with a narrow range of z around the mean.

Chapter 3

The Colour Magnitude Diagram

Once we have the photometric and spectroscopic catalogues, we must correlate them in order to determine the cluster members. We are then ready to make the Colour Magnitude diagrams for our clusters.

The spectroscopic and photometric catalogues were correlated by taking the coordinates of the objects in the spectroscopic masks and converting them to the geometrical system of the photometry catalogue. In a few cases the transformed position of the slit lay outside the area covered by the imaging frame, this only caused the object to be rejected in two cases so it is not a significant problem.

As mentioned in Section 2.2.5, the B-R colour is not yet calibrated and we will do this by using model predictions for the CM slope.

The layout of the chapter is as follows: in Section 3.1 we explain how the models are used to calibrate the B-R colour and locate the red sequence of galaxies in the CMDs. In Section 3.2 we describe the CMDs and give an estimate of the uncertainties. In Section 3.3 the blue fraction of galaxies is calculated for each cluster. Sections 3.4 to 3.7 show the CMD's for each cluster and give tables with the photometric catalogues. Section 3.8 explains how a composite CMD is created by combining the results for all the clusters.

3.1 B-R Calibration: Fitting the CM slope with SPS models.

Since no calibration is available for the B band data, the B-R colours are not calibrated. We will therefore calibrate them by assuming a CM slope and zero point from the Kodama & Arimoto (1997) stellar population synthesis (SPS) models.

These models assume that the CM slope is a metallicity effect and give the evolution of the slope and zero point of the red sequence of galaxies as a function of redshift. The model parameters are adjusted to reproduced the observed CMD of the Coma cluster. These models have been tested and shown to be able to reproduce the CMDs of clusters at different redshifts up to 1.2 (Kodama et al 1998).

We first calculate the predicted slope and zero point of the red sequence for each of the four cluster redshifts. Since our R magnitudes are calibrated, once we have located the predicted red sequence in the B-R versus R diagram, we are simply left with a shift in B-R between our data points and the model red sequence. Now we can shift our data points by a constant value that minimises the dispersion of our red galaxies around the model line. (In this context by red galaxies we mean the ones not showing emission lines, which as it can be seen in the diagrams are the galaxies following the red sequence). By doing this, we see that the predicted red sequence is a good fit to our data points. For three of the four clusters the CM slope given by the model is within 1σ of the slope of a linear fit to the data points for the red galaxies. For one cluster, Cl1633, the slope given by the model is 2.75σ away from the slope of a linear fit to the data points, but it should be noted that the linear fit to the data points is affected by the small number of points. The predicted values for the slope of the red sequence given by the models for each cluster redshift are as follows:

-Cluster ***Cl0819***: z=0.2296. m=-0.0665.

-Cluster ***Cl0849***: z=0.2347. m=-0.0668.

-Cluster ***Cl0841***: z=0.2396. m=-0.0670.

-Cluster ***Cl1633***: z=0.2406. m=-0.0670.

3.2 The CMD's

Once we have calibrated the B-R colours we are ready to show the Colour Magnitude diagrams for each of our four clusters, we do so in Sections 3.4, 3.5, 3.6 and 3.7. In these sections, we also give tables with the R magnitude and B-R colour for the objects for which spectra is available. The identification numbers for each mask are as in the spectroscopy tables given in section 2.3. Figures 3.4, 3.5, 3.6 and 3.7

show the CMD for clusters Cl0819, Cl0841, Cl0849 and Cl1633 respectively. In each CMD, objects spectroscopically confirmed as members have been plotted as filled symbols, and spectroscopically confirmed non-members as open symbols. The different symbols correspond to the different masks , and the numbers next to each symbol correspond to the identification numbers as in the tables for the spectroscopy and photometry for each cluster. In this way we can easily correlate the information in the diagrams with the information in the photometric and spectroscopic tables. Objects which exhibit emission lines are surrounded by a larger circle. The crosses are objects in the photometry catalogue for which spectra is not available. Only objects with *stellarity* parameter less than 0.8 given by *SExtractor* (ie galaxies) are plotted here.

The predicted line for the red sequence given by the models as discussed in the previous section, is plotted in each diagram as a dashed line. It can be seen that the model line is a good fit to the data points corresponding to red galaxies (ie filled symbols not surrounded by a larger circle).

3.2.1 Estimating the Errors in the CMD

Error bars have not been plotted in the CMD figures for clarity, but instead they will be discussed here.

The intrinsic photometry errors for the instrumental magnitudes, in both R and B bands, are small. The values vary from 0.01 magnitudes for the bright galaxies plotted in the CMD's, (this is for galaxies of around R=18 magnitudes), to values around 0.03 for objects of about R=20 (this is roughly the magnitude cut in R in the definition of the blue galaxy fraction, see section 3.3). The internal errors rise as we move to fainter magnitudes, reaching 0.1 for galaxies of around 22 magnitudes in R (these are the fainter objects plotted in the CMD's).

The uncertainties in determining the magnitudes and colours due to the calibration are larger than the internal errors. The R magnitudes were calibrated using standard stars (see section 2.2.5) so we have to take into account the uncertainty in the determination of the zero point, the extinction coefficient and the colour term. The errors of these three parameters calculated by *fitparams* when solving

the transformation equations are given in section 2.2.5, and they introduce an error of 0.08 magnitudes in R when added in quadrature. Therefore the uncertainty in R due to the calibration dominates the internal errors of the photometry in most of the range of R magnitudes plotted in the CMD's.

To calibrate the B-R colours we shifted our data points in order to minimize the dispersion of the red galaxies around the predicted red sequence (see Section 3.1). Hence the uncertainty in the determination of the B-R colours can be estimated by taking into account the uncertainty in the shift that was applied. Since this depends on the number of objects used in fitting the data points to the model line, the uncertainty in B-R varies for each cluster, being 0.02 magnitudes for Cl0819 and Cl0849, 0.04 magnitudes for Cl0841 and 0.03 magnitudes for Cl1633. Therefore for the brighter objects, where the internal errors in B and R are smaller, the uncertainty due to the calibration dominates the total error in the B-R colour. For fainter galaxies, but still in the range considered in the CMD, the internal error grows and dominates over the calibration uncertainty.

3.3 Blue Galaxy Fraction

Having the CMD for each cluster, we can calculate the blue fraction of galaxies following the original definition from BO84. We have to consider galaxies brighter than M_V=-20 in the rest frame, and of those we define as "*blue galaxies*" the ones with a B-V colour bluer than $\Delta(B-V) < -0.2$ from the red sequence of the colour magnitude relation. We need to transform these values to our system. First we have to convert the magnitude cut M_V=-20 in the rest frame to an apparent magnitude R in the observed frame at the corresponding redshift. We can also obtain this information from model predictions, but in this case we will have to use non-evolutionary models since the original criterion from BO84 for the magnitude cut did not consider evolution. M_V=-20 correponds to values of R of 20.58, 20.64, 20.70 and 20.71 for clusters Cl0819, Cl0849, Cl0841 and Cl1633 respectively.

The next step is to convert the colour difference $\Delta(B-V) < -0.2$ in the restframe to a B-R colour at the cluster redshift. According to Fukugita et al. (1995) $\Delta(B-V) = -0.2$ is more or less the difference in colour of a Sab-type

galaxy and a E-type galaxy in the Hubble sequence of the present day galaxies (see also Kodama and Bower 2000). It is then possible to transform the $\Delta(B-V)$ criteria into $\Delta(B-R)$ by using the colour difference of an E and a Sab galaxy at the appropiate redshift. This procedure gives us a value $\Delta(B-R)$=-0.4 at z=0.2 using the galaxy colours in Fukugita et al. (1995).

We use the red sequence calculated in the previous section as a reference zero point from where we can calculate the colour difference $\Delta(B-R)$=-0.4.

The R magnitude cut and the B-R=-0.4 criteria for identifying *"blue galaxies"* are plotted in each CMD as a vertical dashed line and a dotted line respectively. Therefore the *"blue galaxy fraction"* can now be calculated by counting how many galaxies lie below the dotted line and at the left of the vertical dashed line. We will consider the spectroscopically confirmed members to calculate the *"blue galaxy fractions"*.

-Cluster ***Cl0819***: we can see in figure 3.4 that only two galaxies are in the area defined for "blue galaxies". Since there are 21 galaxies brighter than the magnitude cut in R, this makes a blue galaxy fraction of 2/21, or 0.095.

-Cluster ***Cl0849***: figure 3.6 shows that two confirmed members fulfill the requisites to be considered as "blue galaxies", although one of them is very near the dashed line under which a galaxy is defined as blue. 25 galaxies are brighter than the magnitude cut and therefore the blue galaxy fraction is 2/25, or 0.080.

-Cluster ***Cl0841***: as it can be seen in figure 3.5 only one galaxy falls in the "blue galaxy" area. There are 12 galaxies brighter than the magnitude cut and hence the blue fraction is 1/12, or 0.083.

-Cluster ***Cl1633***: in this case there are two "blue" galaxies as figure 3.7 shows. There are 13 galaxies brighter than the magnitude cut, which makes a blue fraction of 2/13, or 0.154

In order to estimate the error on the blue fractions given above, we use Poisson statistics to put limits on the probabilities of getting these fractions. In this way, if the total number of galaxies is n and we find x of them to be blue, we compute the

blue fraction that is consistent within one σ level with the measured blue fraction x/n. Doing this we find the following uncertainties for the blue fractions shown above: Cl0819, 0.095 $\pm$ 0.071; Cl0849, 0.080 $\pm$ 0.060; Cl0841, 0.08 $\pm$ 0.11; Cl1633, 0.15$\pm$0.12.

3.4 Cl0819

Table 3.1: Cl0819 Photometry: id numbers correspond to the spectroscopy identification numbers for Mask1 and Mask2 in tables 2.6 and 2.7 .

Ap Mask1	R	B-R	Ap Mask2	R	B-R
1	20.27	2.18	1	19.93	2.02
2	18.81	2.26	2	19.62	2.69
4	19.20	2.37	3	19.33	2.44
5	19.85	1.95	4	19.90	2.34
6	19.91	2.35	5	19.16	2.40
7	20.45	3.10	6	20.78	2.46
8	19.84	2.55	7	19.78	2.59
9	19.01	2.48	8	19.04	1.88
10	19.02	2.47	9	18.71	2.56
11	19.06	2.34	10	20.16	2.00
12	18.33	2.43	11	19.46	2.09
13	18.86	2.52	12	20.16	1.78
14	18.92	2.49	13	20.09	2.12
15	19.41	2.46			
16	19.18	2.59			
17	18.99	2.41			
18	19.11	2.48			
19	20.58	2.15			
20	19.38	1.88			
21	19.11	2.59			
22	20.56	1.69			
23	19.37	2.37			
24	19.22	1.52			
25	19.15	2.28			
26	19.49	2.83			

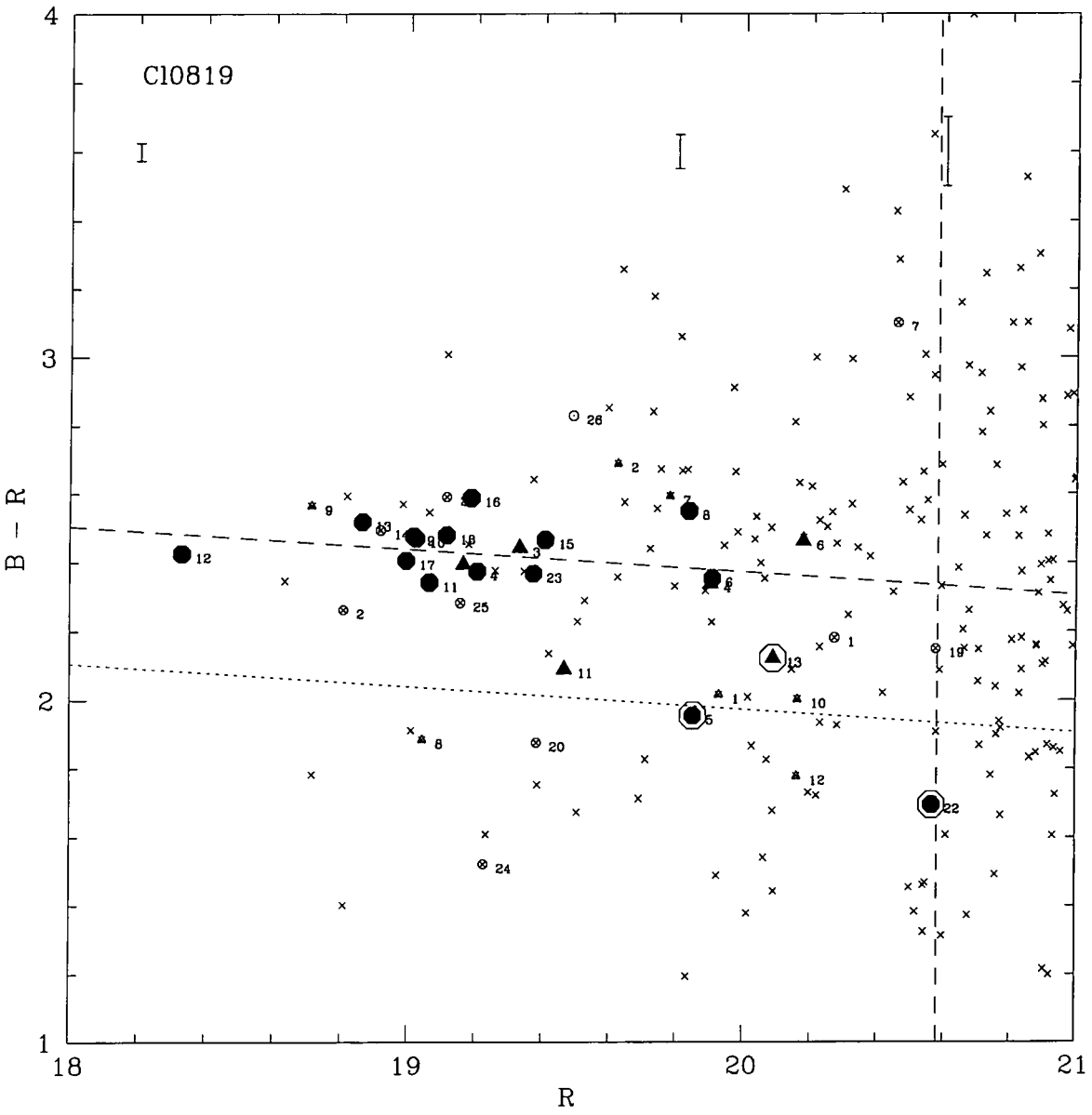

Figure 3.1: Colour-Magnitude Diagram for Cl0819. Circles are objects with spectra from Mask1, triangles are objects with spectra from Mask2. Filled symbols are cluster members and objects which exhibit emission lines are surrounded by a circle. The id number correspond to the id numbers given in the photometry and spectroscopy tables.

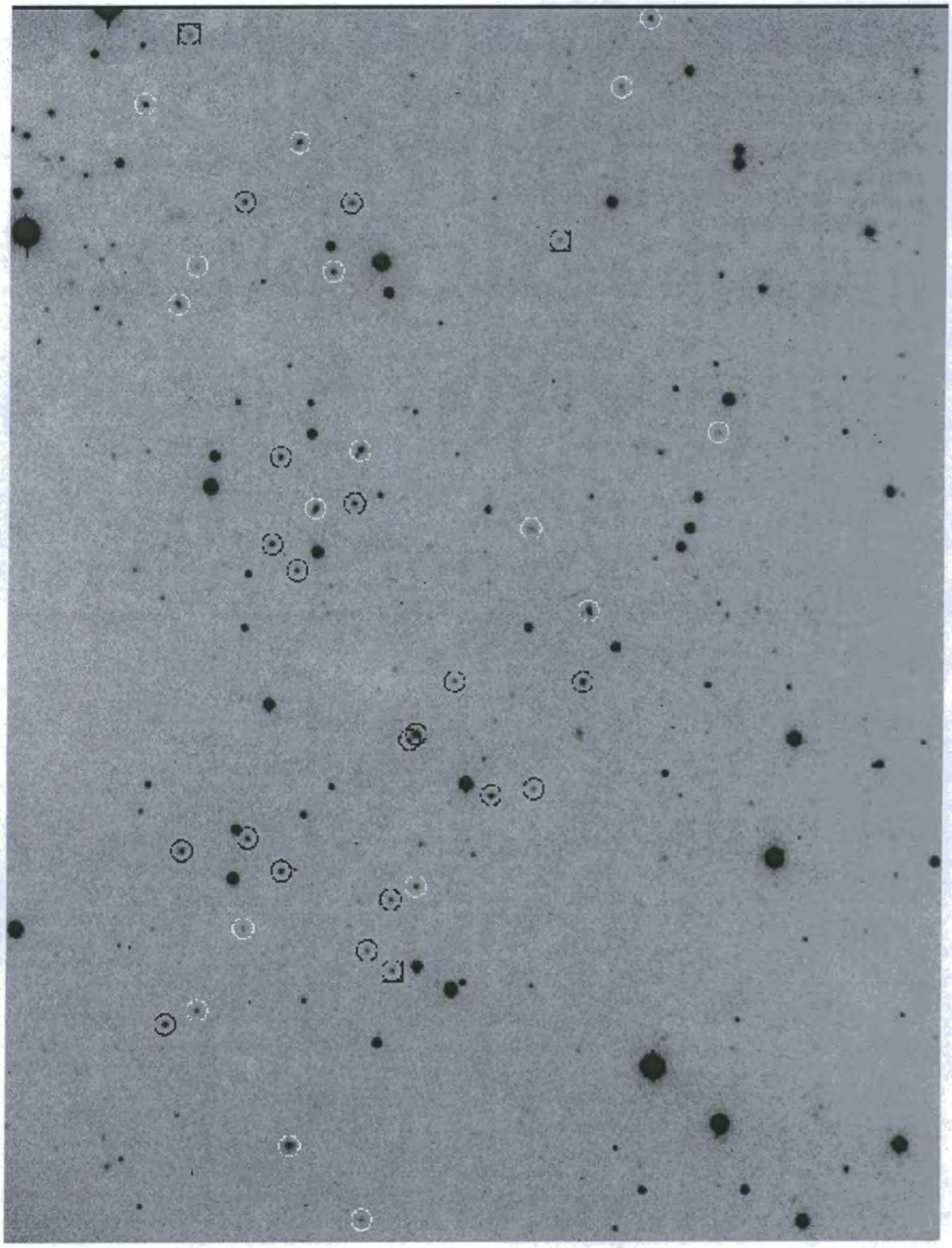

Figure 3.2: Cl0819 field. Here, objects for which spectra are available are circled. Black circles indicate objects for which the spectra confirms membership to the cluster. Objects surrounded by a square symbol are members showing emission lines. This is an R image of Cl0819 covering an area of 8 × 11 arcmin.

3.5 Cl0841

Table 3.2: Cl0841 Photometry: id numbers correspond to the spectroscopy identification numbers for Mask1 and Mask2 in tables 2.8 and 2.9 . Apertures 2+3, 4+5+6, 11+12 in Mask2 are objects that can not be separated as different objects in the photometry but for which more than one redshift was obtained from the spectra of a single slit in the mask.

Ap Mask1	R	B-R	Ap Mask2	R	B-R
1	19.56	2.60	1	21.70	2.22
2	21.00	1.72	2+3	20.71	3.28
3	20.90	2.17	4+5+6	18.52	2.42
4	19.97	2.57	7	20.83	2.27
5	20.86	1.72	8	18.31	2.69
6	20.53	1.68	9	19.99	2.52
7	20.64	2.39	10	20.32	2.23
8	20.04	2.20	11+12	20.75	2.36
9	19.30	2.45	13	19.79	1.22
10	18.87	2.50	14	20.80	2.14
11	22.53	1.70			
12	21.15	2.17			
13	19.63	2.66			
14	21.23	2.61			
15	21.52	1.81			
16	21.88	1.09			
17	21.39	1.45			
18	20.17	2.39			
19	20.38	1.93			
20	20.93	1.79			
21	20.03	1.93			

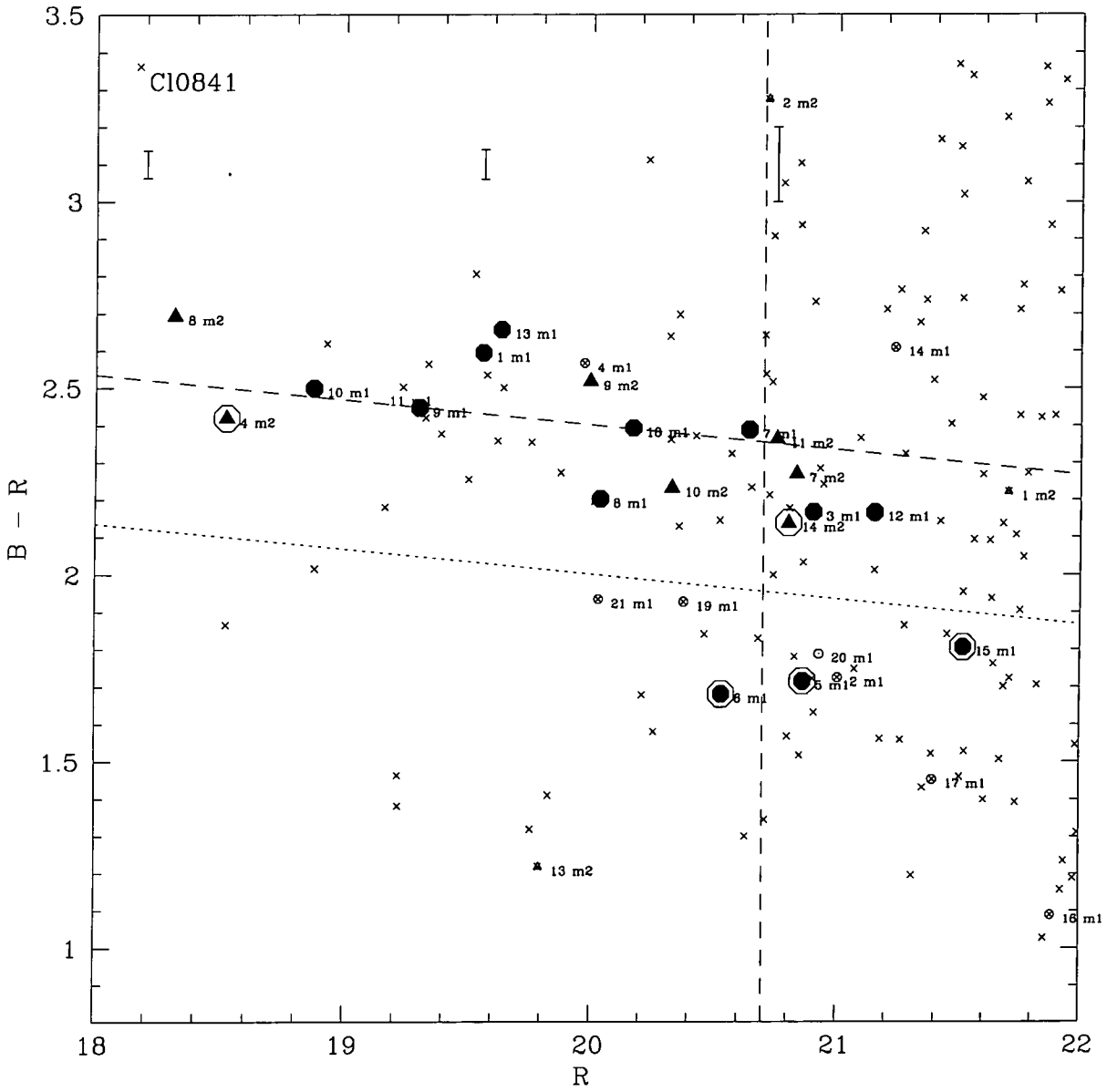

Figure 3.3: Colour-Magnitude Diagram for Cl0841. Circles correspond to objects with spectra from Mask1, triangles are objects with spectra from Mask2. Members are filled symbols and objects showing emission lines are surrounded by a circle. The id numbers correspond to id numbers in the tables for the spectroscopy and photometry.

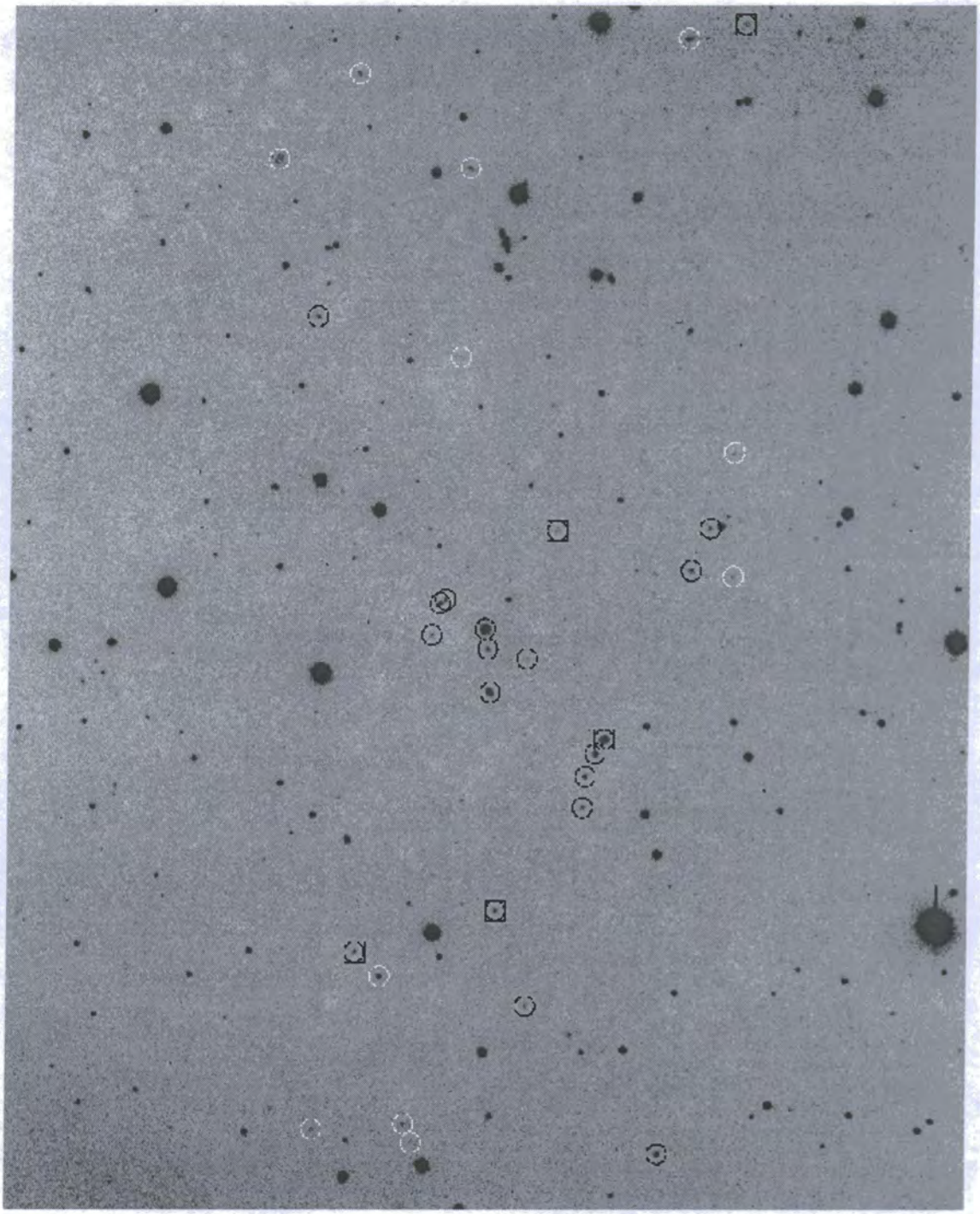

Figure 3.4: Cl0841 field. Objects with spectra are circled. Objects spectroscopically confirmed as members are indicated by black circles and objects with emission lines are surrounded by a square. This image covers 9 × 11 arcmin.

3.6 Cl0849

Table 3.3: Cl0849 Photometry: id numbers correspond to the spectroscopy identification numbers for Run1-Mask1 (R1 M1), Run2-Mask1 (R2 M1) and Run2-Mask2 (R2 M2) in tables 2.10, 2.11 and 2.12 . ID for which magnitudes are not given, correspond to apertures in the spectroscopy masks falling outside the area covered by the photometry image. This happened for 4 objects: ID 1, 2 and 3 from Run1-Mask1 (which coincide with ID 1 Run2-Mask1, ID 1+2 Run2-Mask2 and ID 3 Run2-Mask1 respectively), and ID 2 from Run2-Mask1.

ID R1 M1	R	B-R	ID R2 M1	R	B-R	ID R2 M2	R	B-R
4	19.63	2.00	4	19.63	2.00	3	18.02	1.49
5	19.14	1.95	5	19.21	2.53	4	18.46	2.43
6	19.73	2.46	6	19.73	2.46	5	19.91	2.31
7	19.49	2.45	7	19.49	2.45	6	19.00	2.64
8	18.71	2.48	8	18.71	2.48	7+8	18.63	2.18
9	18.46	2.43	9	19.72	2.37	9	18.85	2.46
10	19.91	2.31	10	18.59	2.49	10	19.64	2.32
11	18.99	2.53	11	18.99	2.53	11	18.89	2.08
12	19.66	1.45	12	19.66	1.45	12	19.41	1.62
13	18.39	2.40	13	18.39	2.40	13	19.83	3.37
14	18.74	2.31	14	18.74	2.31	14	19.70	3.20
15	17.66	2.65	15	17.66	2.65	15	19.67	2.74
16	18.25	2.56	16	18.25	2.56			
17	18.52	2.17	17	18.52	2.17			
18	19.67	2.14	18	19.67	2.14			
19	19.59	2.05	19	19.59	2.05			
20	19.96	3.56	20	19.96	3.52			
21	20.18	3.14	21	18.88	2.42			
22	18.88	2.42	22	19.56	1.93			
23	19.38	2.28	23	19.33	2.50			
24	19.56	1.93	24	19.31	2.91			
25	19.00	2.42	25	20.16	2.37			
26	19.33	2.50	26	18.96	2.04			
27	19.31	2.91						
28	20.16	2.37						
29	18.96	2.04						

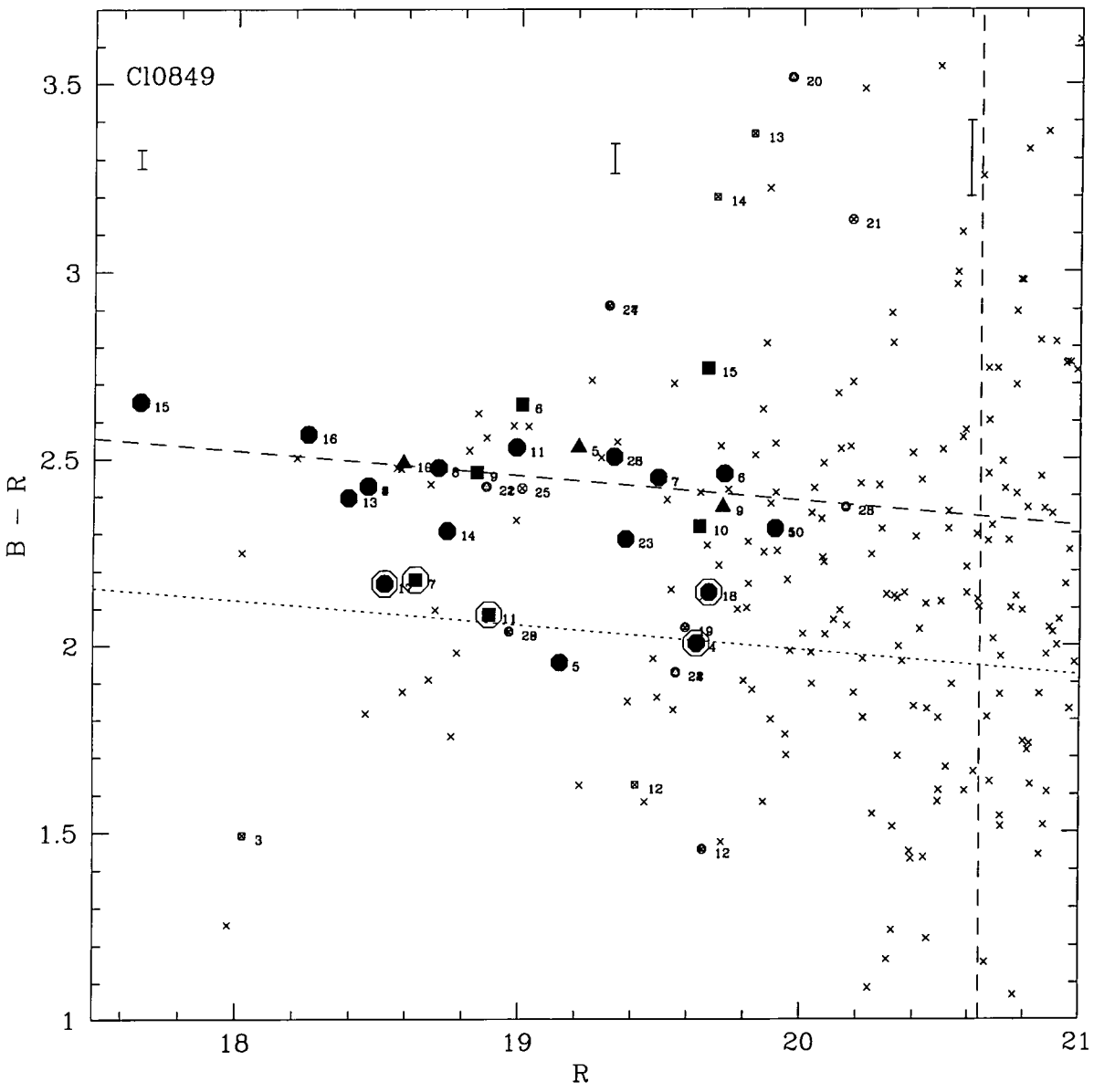

Figure 3.5: Colour-Magnitude Diagram for Cl0849. Circles, triangles and squares are objects with spectra from Run1-Mask1, Run2-Mask1 and Run2-Mask2 respectively. Filled symbols represent cluster members and objects surrounded by a circle are those showing emission lines. The id numbers correspond to the numbers in the photometry and spectroscopy tables.

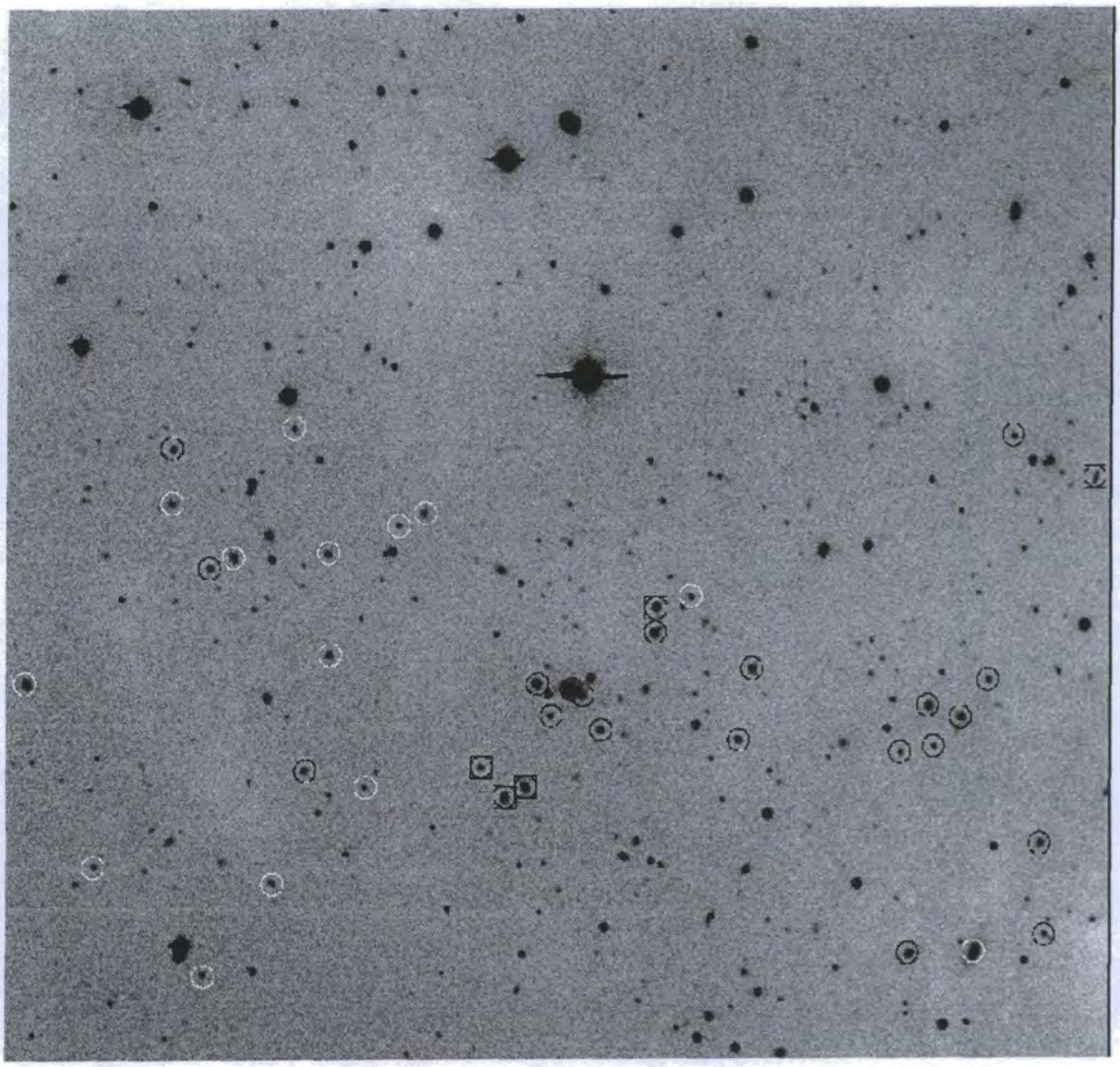

Figure 3.6: Cl0849 field. Objects for which spectra are available are circled. Objects spectroscopically confirmed as members are indicated by black circles and objects with emission lines are surrounded by a square. This image coverr an area of 10 × 8.5 arcmin.

3.7 Cl1633

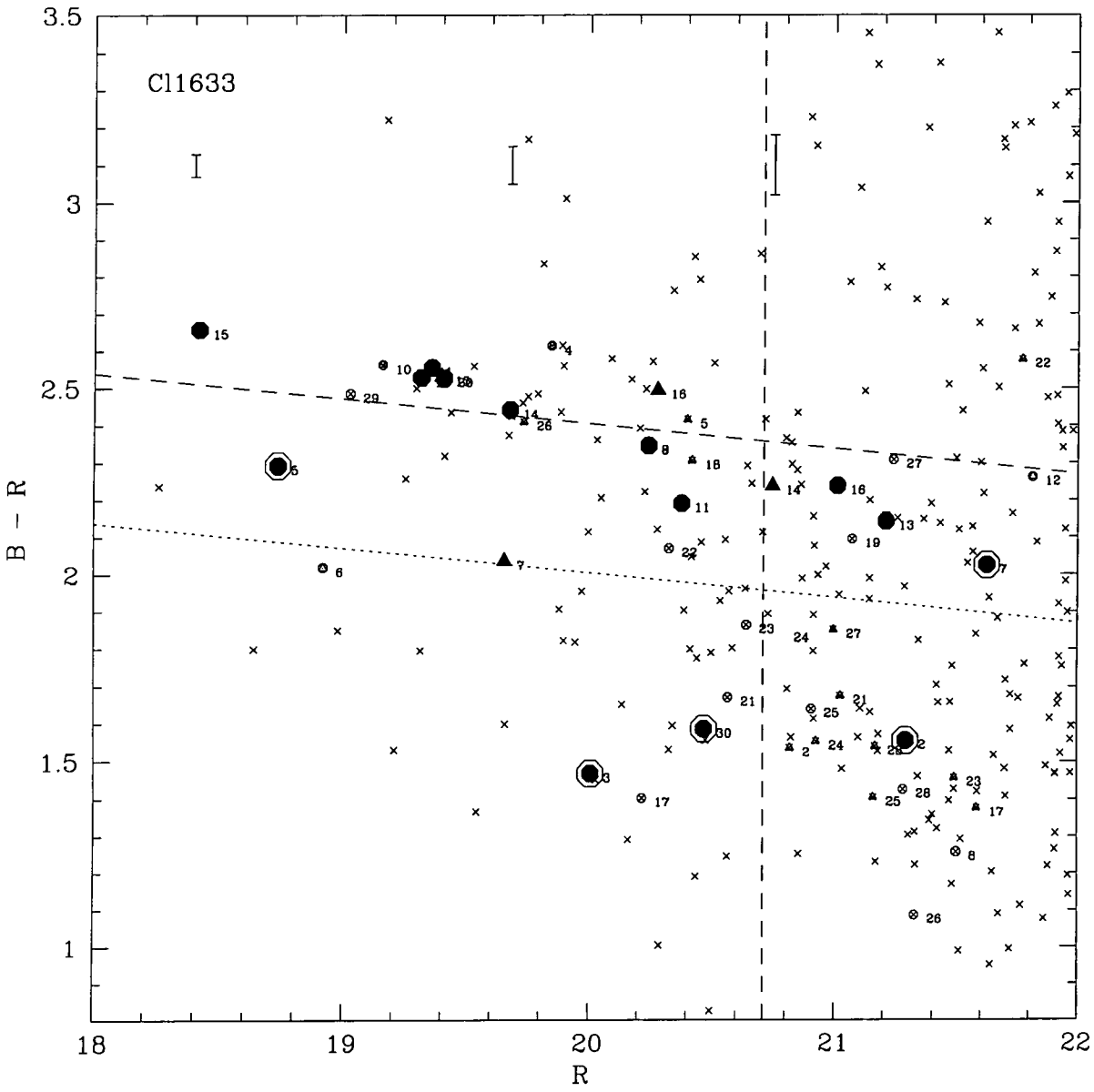

Figure 3.7: Colour-Magnitude Diagram for Cl1633. Circles are objects with spectra from Mask1 and triangles objects with spectra from Mask2. Cluster members are filled symbols and objects with emission lines are surrounded by a circle. The id numbers correspond to numbers given in the photometry and spectroscopy tables.

Table 3.4: Cl1633 Photometry: id numbers correspond to the spectroscopy identification numbers for Mask1 and Mask2 in tables 2.13 and 2.14. ID's 8+9 and 18+19+20 in Mask2 correspond to objects that can not be separated as different objects in the photometry but for which more than one redshift was obtained from the spectra of a single slit in the mask.

ID Mask1	R	B-R	ID Mask2	R	B-R
1	19.36	2.56	1	19.36	2.56
2	21.29	1.56	2	20.82	1.53
3	20.01	1.47	3	20.01	1.47
4	19.84	2.61	4	19.84	2.61
5	18.74	2.29	5	20.40	2.42
6	18.92	2.02	6	18.92	2.02
7	21.62	2.02	7	19.66	2.04
8	21.50	1.26	8+9	20.24	2.34
9	20.24	2.34	10	19.16	2.56
10	19.16	2.56	11	20.38	2.19
11	20.38	2.19	12	21.81	2.26
12	21.81	2.26	13	21.21	2.14
13	21.21	2.14	14	20.75	2.24
14	19.68	2.44	15	19.40	2.53
15	18.42	2.66	16	20.28	2.49
16	21.01	2.24	17	21.58	1.38
17	20.22	1.40	18+19+20	20.42	2.30
18	19.32	2.53	21	21.02	1.67
19	21.07	2.09	22	21.77	2.58
20	19.41	2.53	23	21.49	1.46
21	20.57	1.67	24	20.93	1.55
22	20.33	2.07	25	21.16	1.40
23	20.64	1.86	26	19.73	2.41
24	21.40	0.78	27	20.99	1.85
25	20.91	1.64	28	21.17	1.54
26	21.33	1.09			
27	21.24	2.31			
28	21.28	1.42			
29	19.03	2.48			
30	20.47	1.59			

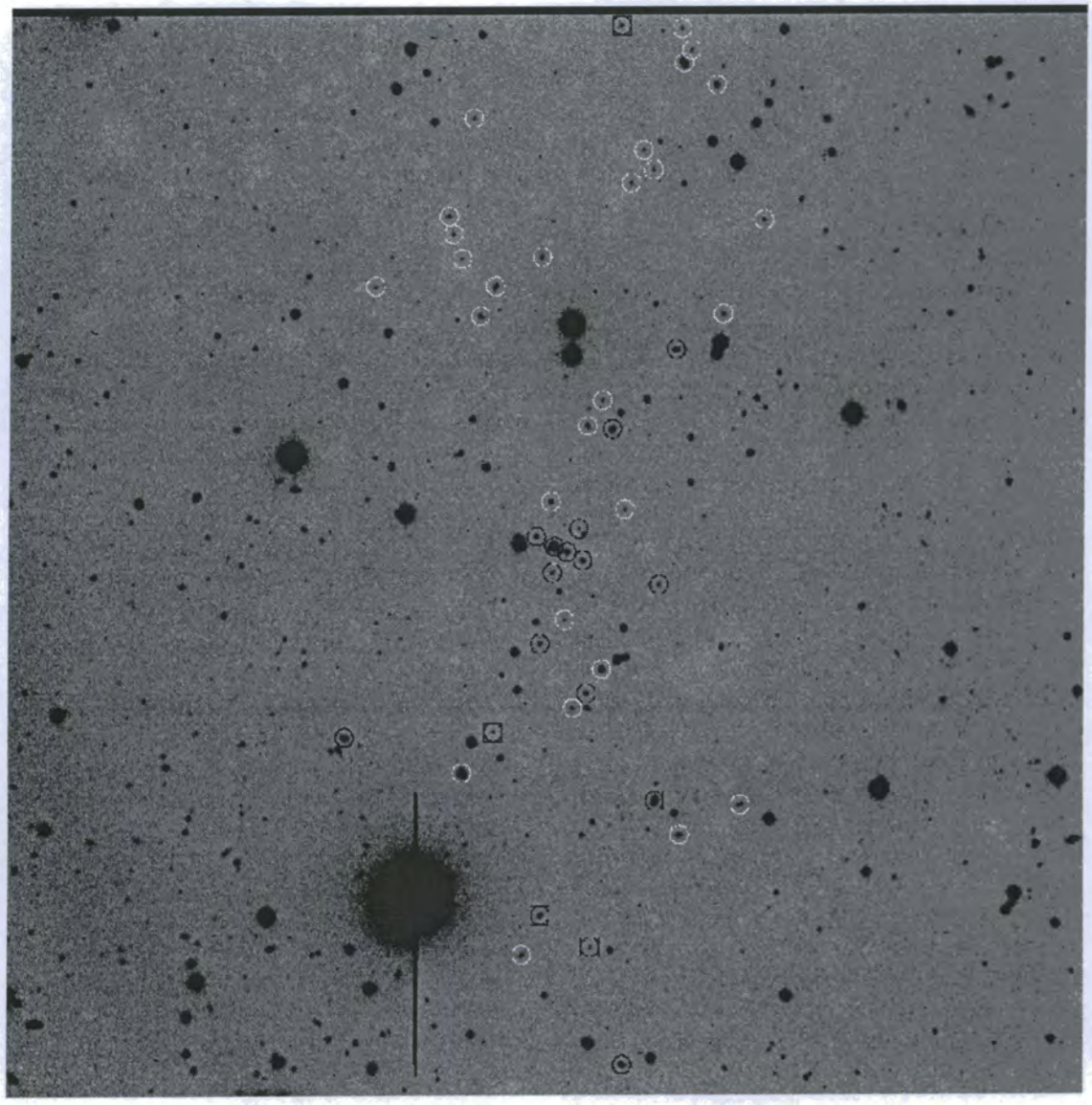

Figure 3.8: Cl1633 field. Objects with spectra are circled. Objects spectroscopically confirmed as members are indicated by black circles and objects with emission lines are surrounded by a square. This image covers an area of 9 × 10 arcmin.

3.8 The Composite CMD

Another approach to studying the blue fraction of galaxies in such "poor" clusters is to create a composite cluster by co-adding all the galaxies into a single Colour Magnitude Diagram. In this way we will have more "cluster members". In order to do this, we first have to take into account the effects of the different cluster redshifts on the magnitudes and colours of the galaxies. Cluster Cl0819, at z=0.2296 (z_{ref}) was chosen as the reference, therefore the CMDs of the other three clusters have to be converted into the equivalent at this redshift value. This can be done again by using the Kodama & Arimoto (1997) models (see Sections 3.1 and 3.2), which give the evolution of magnitudes with redshift, to convert our R magnitudes into the corresponding magnitude at the reference redshift. This is equivalent to shifting the x-axis of each CMD.

In order to transform the B-R colours to the corresponding values at the reference redshift, we apply the same method that we explained in section 3.1 to calibrate the B-R colours by using the model predictions. Therefore we shift the data points in B-R by a value that minimizes the scatter around the predicted red sequence at the reference redshift.

The composite CMD is shown in figure 3.8. Different symbols have been used to plot galaxies for each different cluster and, as before, galaxies exhibiting emission lines are surrounded by a larger circle. The red sequence, magnitude cut and criteria for defining blue galaxies are the same as for Cl0819 (since this is the cluster we chose as a reference for the redshift value).

We can now calculate the blue galaxy fraction by looking at figure 3.8, which shows that there are six objects in the area that defines blue galaxies. The number of galaxies brighter than the magnitude cut is 71, and therefore the "blue galaxy fraction" for the composite cluster is 6/71, or 0.084.

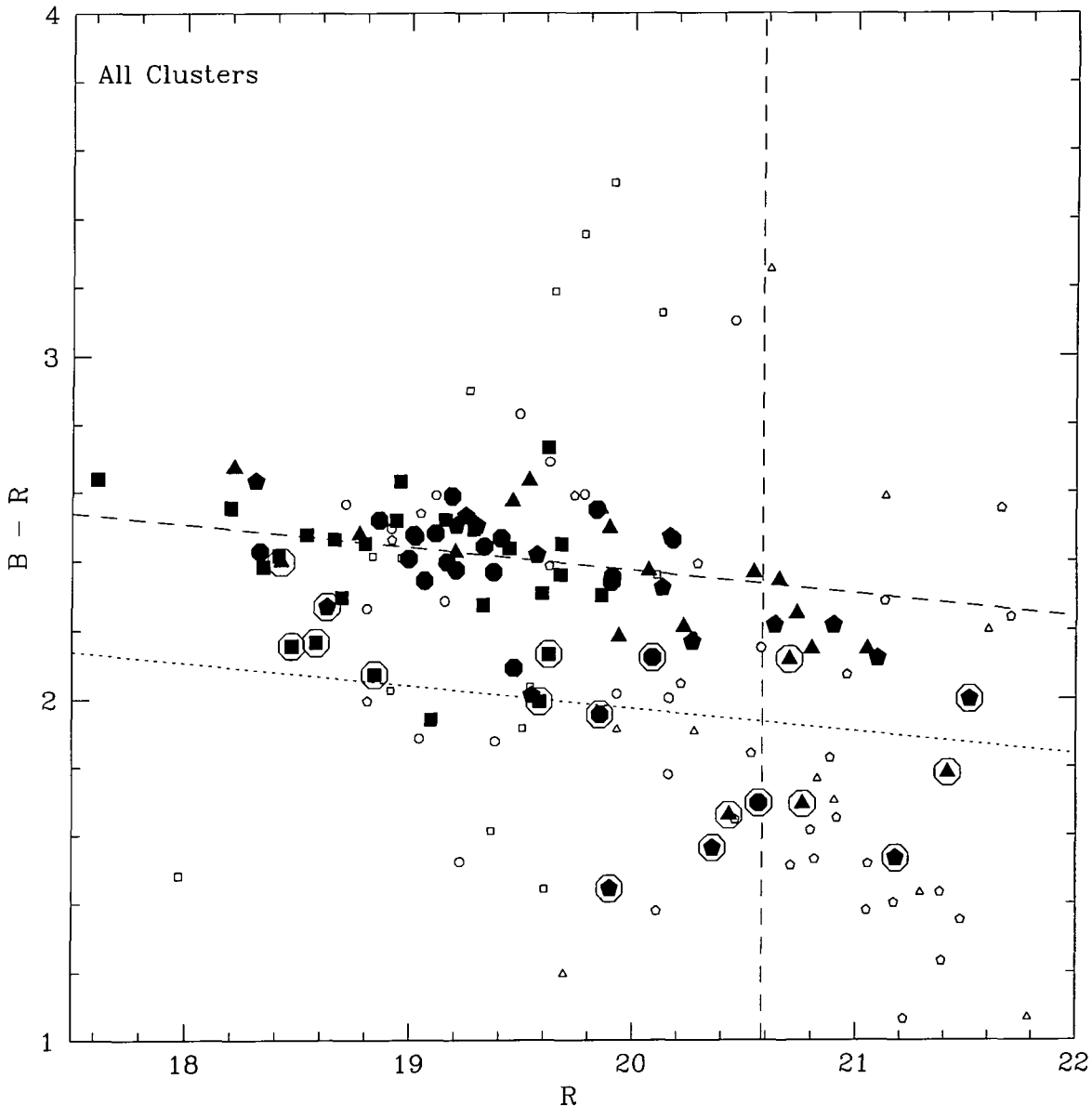

Figure 3.9: Colour-Magnitude Diagram for the "composite cluster". The different symbols correspond to galaxies from different clusters: circles are Cl0819 members, triangles are members of Cl0841, squares correspond to Cl0849 and pentagons to Cl1633. Objects showing emission lines are surrounded by a circle.

3.9 Summary

In order to make the discussion and comparison with other results from the literature easier in Chapter 5, we summarise the results in table 3.9, where we show the main characteristics of each cluster (z, L_X) and the value of the blue fraction that we have calculated.

Cluster	$L_X(10^{43} erg/s)$	z	f_b
Cl0819	1.38	0.2296	0.095±0.071
Cl0841	1.34	0.2396	0.08±0.11
Cl0849	2.11	0.2347	0.08±0.06
Cl1633	0.53	0.2406	0.15±0.12
Composite	-	z_{ref}	0.084

Table 3.5: Summary table: Characteristics of the clusters and values of the blue fraction. z_{ref} refers to the reference redshift used to make the composite cluster (ie same redshift as Cl0819).

3.10 Some points to address

The blue fractions in the previous discussion have been measured taking into account spectroscopic members only. However, our spectroscopic completeness will not significantly affect the values we have derived for the blue fractions, since the fraction of blue galaxies which have spectra is comparable to the fraction of red galaxies with spectra. For example, the fraction of blue galaxies with spectra above the magnitude cut (R<20.58) for cluster Cl0841 is about 30%, the corresponding fraction for red galaxies is about 27%. Therefore, neither the red or blue galaxies are over-represented in our magnitude-limited sample.

A second point that has to be addressed is the fact that our blue galaxy fractions have been calculated following the original BO84 definition except for one thing. In BO84 only blue galaxies within R_{30} (the radius from the cluster centre that contains 30 percent of the cluster population) are considered. This condition has not been applied in our case because, unlike BO, we are studying poor clusters which have numerically fewer galaxies and therefore the R_{30} criterion becomes invalid due to the small numbers. However we have assumed a fixed linear size (which corresponds approximately to 4 arcminutes at z=0.2) and therefore the same physical region for all the clusters has been studied.

Chapter 4

HST Data: Morphological Analysis

A key piece of information to understand the evolution of galaxies in clusters, and which mechanisms are causing this evolution, is the morphology of the cluster population. As pointed out in Chapter 2, our sample of clusters has been observed by HST with the purpose of having an accurate morphological classification of the cluster population. We have HST images for eight of the nine clusters in our sample; Cl1633 is the cluster for which an image is not available.

In this chapter I will show the HST images for the three clusters of our subsample: Cl0819, Cl0841 and Cl0849. I made these mosaic HST images of our clusters, however the morphological analysis of these data has been done by Michael Balogh. Here I will give a brief description of the procedure followed to obtain the morphological parameters using GIM2D on the HST images, and will show the results from the morphological analysis of the clusters we are considering.

4.1 HST Images

In this section we show the HST mosaic images for Cl0819, Cl0841 and Cl0849. For each cluster three images in the F702w filter were obtained, with exposure times ranging from 2100 to 2600 seconds per exposure. The three images of each cluster were offset by about 10 pixels and during the reduction procedure they were aligned and added to remove cosmic rays and hot pixels. The images were not dithered or regridded because this does not preserve the noise characteristics of the pixel, and the surface brightness fitting software that we will use for the morphological analysis is sensitive to the regridding pattern.

We show now the mosaic images of our clusters and in each image, we indicate

the measured redshift and the id number of galaxies with available spectra. These id's correspond to the ones given in the spectroscopy and photometry tables given in Chapters 2 and 3.

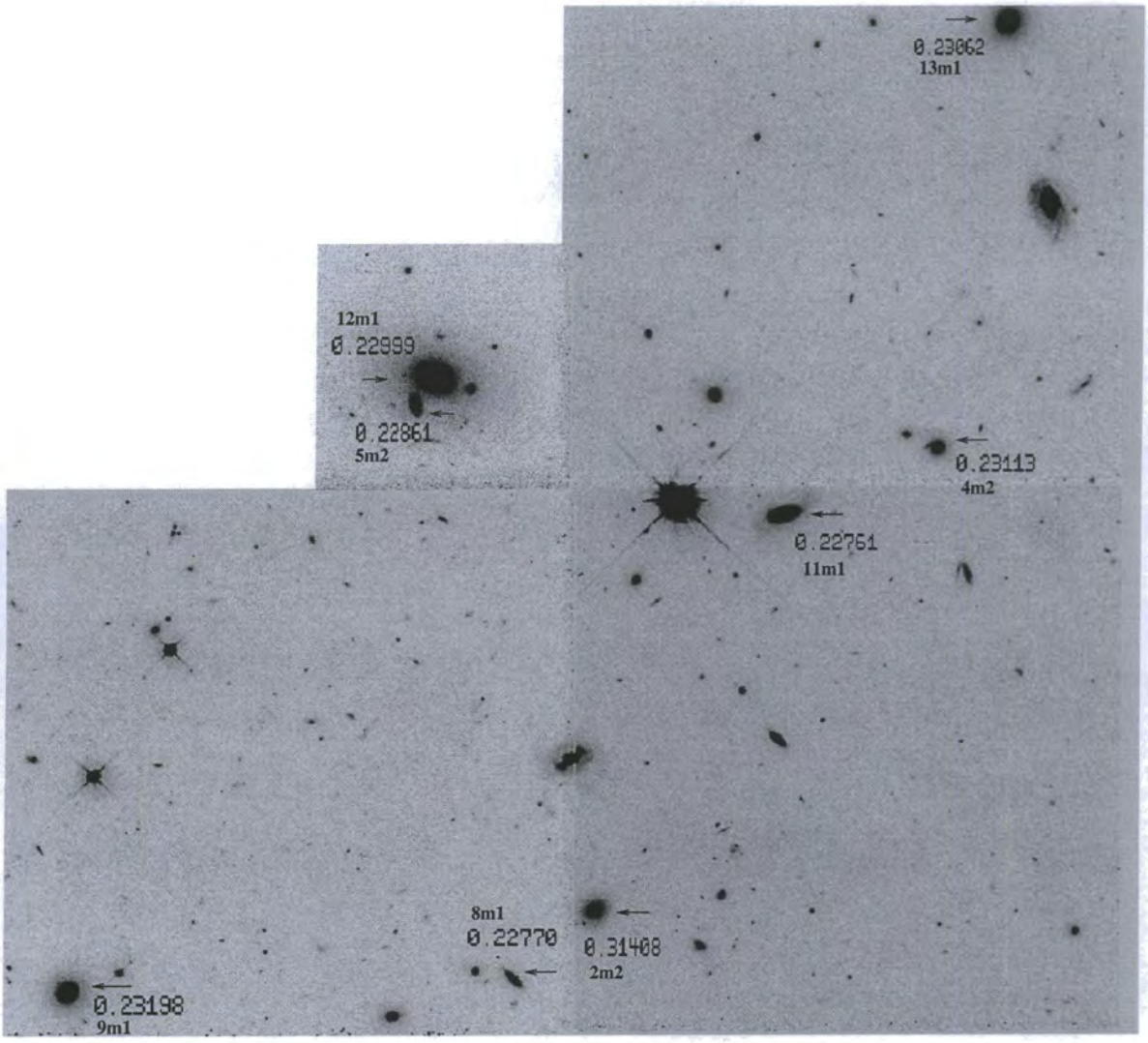

Figure 4.1: HST image of Cl0819.

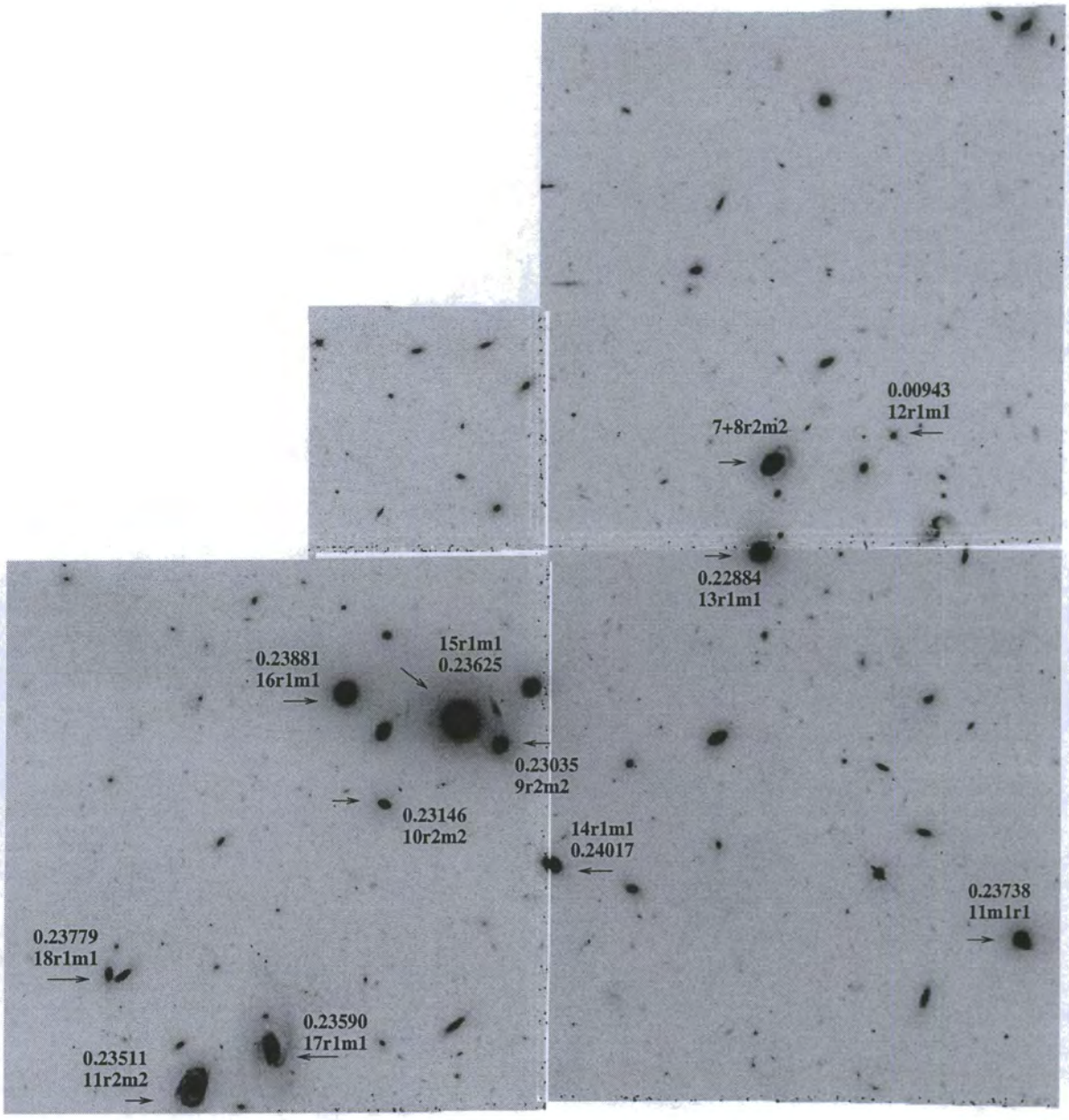

Figure 4.2: HST image of Cl0849.

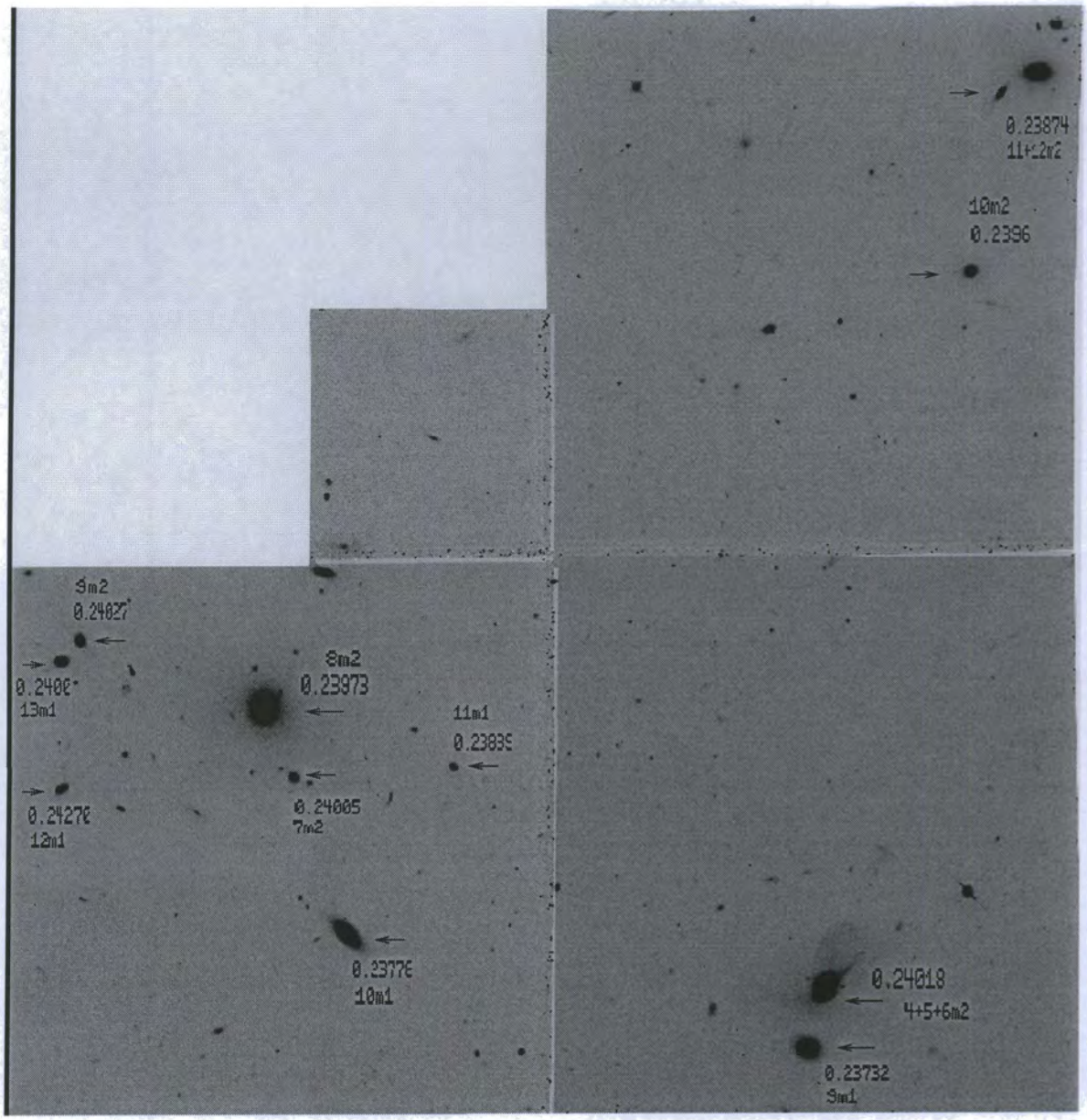

Figure 4.3: HST image of Cl0841.

4.2 Morphological Analysis

Here we will give a brief summary of the procedure followed to analyse the HST images and we will show the results for our three clusters.

The IRAF package GIM2D written by Luc Simard was used to determine the morphological parameters for galaxies brighter than $r = 22.8$. The full details of this program are given in Simard et al. (2000, in preparation) and descriptions can also be found in Tran et al. (2000, ApJ in press, astro-ph/0010278) and Marleau & Simard (1998, ApJ 507, 585).

From the original HST image, the individual galaxies are extracted with SExtractor, and the segmentationimage is used to define which pixels belong to the galaxy that is being analysed.

Each galaxy model is fit with a "bulge" and "disc" component, and it is represented by up to twelve parameters. Details of the fitting parameters are given in Balogh et al. (2001, in preparation). We choose to fit the disc with an exponential profile, and the bulge with a deVaucoleurs profile. GIM2D then searches for the best fit solution in the parameter space using the Metropolis alogorithm, which is inefficient but does not easily get "trapped" in local minima.

The two component (disc and bulge) model is a simplified approximation to the real structure of a galaxy. The distinction between a "disc" and "bulge" component is made only on the surface brightness profile, and does not necessarily correspond to kinematically distinct components. For this reason, we will use the terminology of Simard et al. (2000) and refer to these components as the photodisc and photobulge.

Using this procedure, morphological parameters were obtained for the three clusters we are considering in this thesis for which *HST* images are available (Cl0819, Cl0841 and Cl0849). We also obtained *HST* images of the rich cluster Abell 2390 ($z = 0.23$) from the archive, recalibrated "on-the-fly" by the Canadian Astronomical Data Centre (CADC). We use this cluster as an example of a "typical" rich cluster against which to compare our data. These images are taken in the f814W filter, rather than the f702W filter in which the images of our clusters were obtained. Although this will likely mean the A2390 galaxies appear systematically more regular, it is unlikely to have a strong effect on the bulge-to-disc ratio. These effects are

discussed in more detail in Balogh et al. (2001). In figure 4.4 we show the distribution of B/T ratios in each of our three poor clusters, and also for Abell 2390, a rich cluster at similar redshift. For the galaxies in the poor clusters, we consider galaxies brighter than $f702W = 22.8$; the equivalent limit for Abell 2390 is $f814W = 22.4$ (the typical colour of an S0 galaxy at $z = 0.2$ is $f702W - f814W = 0.45$, Fukugita et al. 1995).

We exclude only objects with half-light radii less than 1 pixel (which are stars), and no other restrictions regarding how good is the fit or related to the symmetry, are imposed. The number given in each panel of figure 4.4 shows the fraction of the light in each cluster which is contained in disc components.

It is obvious from the figure that the population of our poor clusters mainly consists of discs. It becomes clear from the comparison of the figures for the poor clusters and the rich cluster A2390, that the morphology of the population differs. At redshift $z \sim 0.2$ we find that poor clusters have a higher fraction of low B/T systems than rich clusters.

The meaning of these results will be discussed in Chapter 5, and they will help us understand how galaxies evolve in poor clusters and which mechanisms are acting in these environments to create the observed morphological fractions.

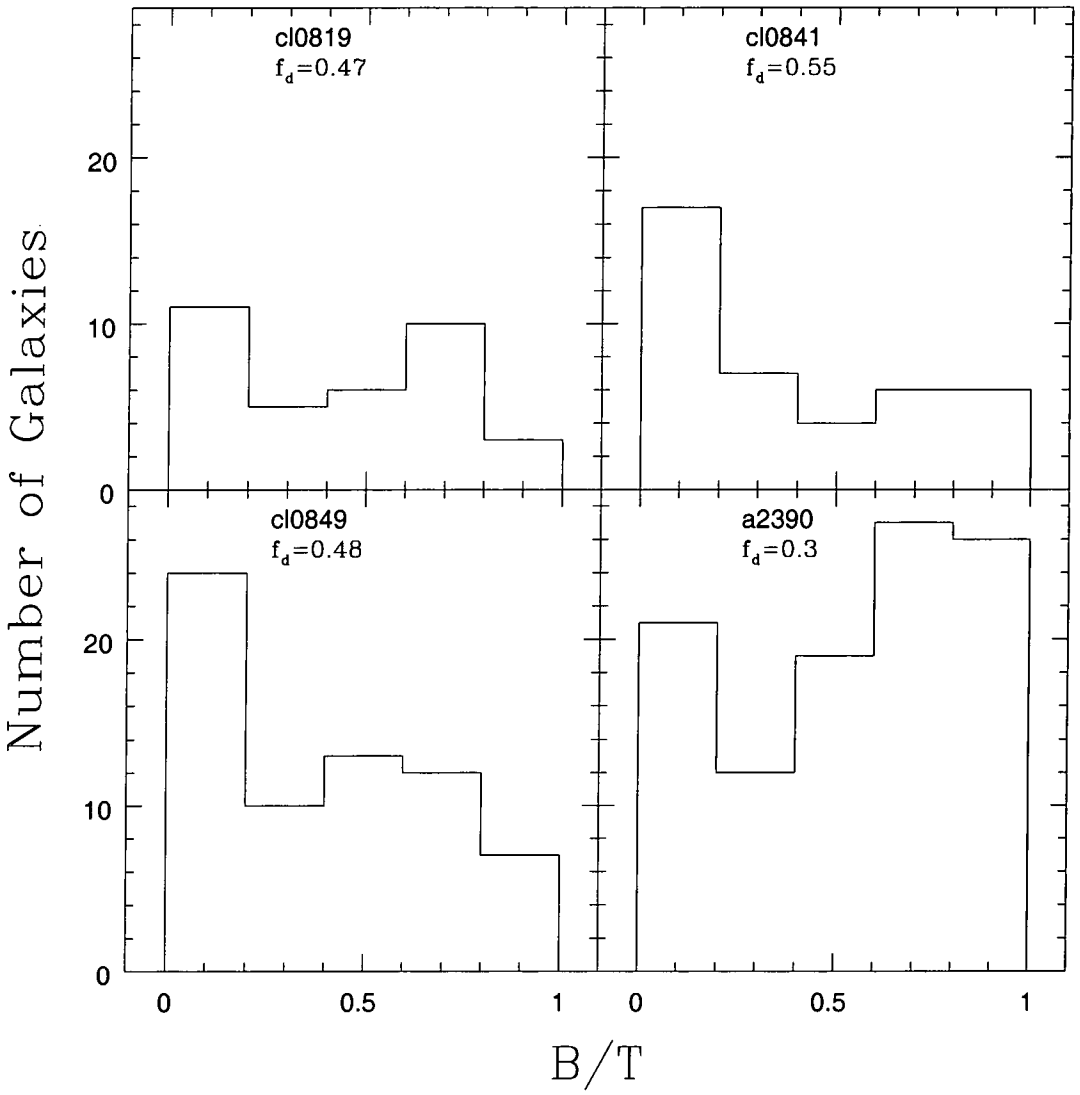

Figure 4.4: Distribution of B/T ratios in three of our poor clusters and the rich cluster A2390 for comparison. f_d is the total luminosity within disc components.

Chapter 5

Discussion: Comparison with Rich Clusters

As discussed in the introduction of this thesis, the purpose of this project was to compare our results regarding the evolution of galaxies in low density environments with the existing results for the denser environments of rich clusters, with the aim of distinguishing between the different mechanisms that cause the transformation of the galaxy population. In this chapter we will look into more detail at the different candidate processes, and will analyse the meaning of our results in the context of the different scenarios.

In Section 5.1 we summarize the existing results regarding the blue fraction of galaxies in rich clusters. In Section 5.2 we compare our results for the blue fraction in our poor clusters with the results for rich clusters. In Section 5.3 we review the candidate mechanisms proposed to transform the galaxy population in clusters, and discuss the implications of our results within the different scenarios. The conclusions are summarized in Section 5.4.

5.1 Blue Fraction: Rich Clusters

In the introduction to this thesis, we summarized the results that different authors find for the blue fraction of galaxies when analysing the galaxy populations of clusters. The original result from Butcher and Oemler (1984) indicated an increase of the blue fraction from 0.03 at $z < 0.1$ to 0.25 at $z = 0.5$. In section 1.2 we pointed out that although a general trend exists with redshift, there are discrepancies between different samples, specially in the redshift range z=0.2 to z=0.3. In

this range of redshifts the value from the original BO84 work is around 0.10 to 0.15. Margoniner and Carvalho (2000) find blue fractions varying from 0.121 $\pm$ 0.029 to 0.233 $\pm$ 0.054, which agrees with values found by Rakos and Schombert (1995, 1996). However the Smail et al. (1998) results at this redshift are lower, with a median of 0.04 $\pm$ 0.02 . Kodama and Bower (2000) find values of the blue fraction consistent with the original results from Butcher and Oemler. It could be argued that the differences could be due to biases in the sample selection. As we discussed in section 1.2, although the samples are composed by rich clusters, the selection criteria is not a common one, and X-ray luminosities are not always given. From the samples mentioned above, only Smail et al (1998) and Kodama & Bower (2000) samples are X-ray selected. Another fact that can lead to differences in the measurement of the blue fraction, is the way in which "blue galaxies" are defined. The original definition from BO84 is not always adopted, which makes it very difficult or impossible to compare different studies. This happens, for example, with a recent interesting result regarding the relationship between blue fraction and cluster richness found by Margoniner et al. (2000b). They study a sample of 295 Abell clusters of all richnesses, and conclude that the blue fraction tends to be higher for poor clusters than for rich clusters at the same redshift. But the authors stress that these results can not be compared to values of the blue fraction calculated following the original definition of BO84, because of different magnitude ranges used in the calculation, which moves the magnitude cut to fainter magnitudes. This naturally leads to higher blue fractions due to the fact that the number of blue galaxies is higher at fainter magnitudes. The relation between blue fraction and richness is observed considering the projected galaxy number density, N, and the authors mention that when restricting the sample to the 11 clusters with available measurements of X-ray luminosities, they do not find any trend between blue fraction and L_X.

Taking these problems into account, and since we are interested in comparing rich and poor clusters, we will concentrate on the samples that have available X-ray luminosities and use the original BO84 definition for the blue fraction. Then the blue fraction for rich clusters at redshift $z \sim 0.2 - 0.3$ varies from the values found by Smail et al (1998) and Kodama & Bower (2000), this is, in the range 0.04 to 0.15.

5.2 Blue Fraction: Our Results versus Rich Clusters

In Chapter 3 we found the following blue fractions for our poor clusters: Cl0819 0.095±0.071; Cl0841 0.08±0.11; Cl0849 0.08±0.06; Cl1633 0.15±0.12 (see table 3.9). Here we will compare these values with the blue fractions found for rich clusters at similar redshifts.

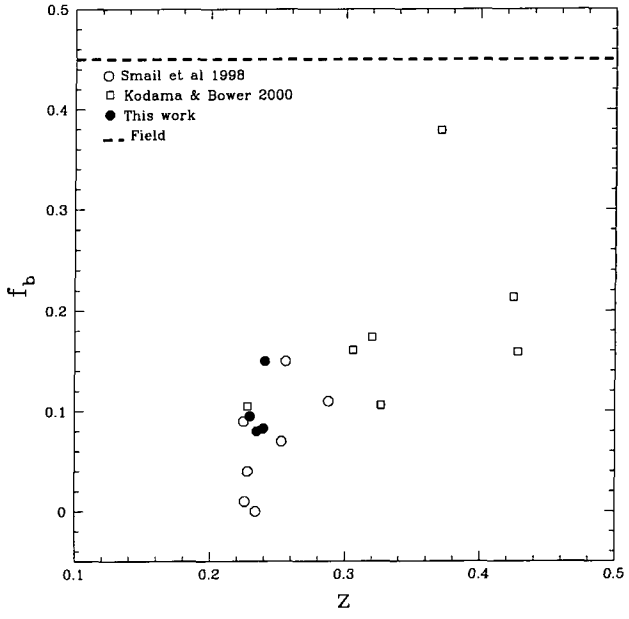

Figure 5.1: Comparison of the blue fraction versus redshift for our clusters and the rich clusters in the X-ray selected samples of Smail et al. (1988) and Kodama & Bower (2000).

Since we are interested in comparing rich and poor clusters, it is easier to compare samples which are X-ray selected. As pointed out in the previous section only two rich cluster samples have been X-ray selected, these are Smail et al (1998) and Kodama and Bower (2000) samples. Our clusters have an X-ray luminosity an order of magnitude smaller than these samples, but our values of the blue fraction fall between the values found in these samples. This can be seen in figure 5.2, where the blue fractions from the three samples have been plotted as a function of redshift. From the figure it is clear that our values for the blue fraction in poor clusters are

similar to previous results for rich X-ray selected clusters, and consistent at the 1σ level (error bars are not shown in the figure for clarity, but the errors are given above in the text). Therefore, from our results we can not conclude that there is a correlation between blue fraction and X-ray luminosity in clusters of galaxies.

It is worth emphasizing that since our values for the blue fraction are similar to those found in rich clusters at this redshift, they are therefore much lower than typical values of the blue fraction in the field. The luminosity function of blue and red galaxies in the field has been determined by the Canada-France Redshift Survey (CFRS, Lilly et al. 1995). The colour division in this study is based on the typical colour of Sbc galaxies, similar to the Butcher-Oemler definition of a blue galaxy. From their luminosity functions at $0.2< z <0.5$, we calculate that the ratio of blue to red galaxies is 0.45, which we take to be the value of the blue fraction in the field. Hence, the blue fraction in our poor clusters is clearly lower than in the field, and very similar to the one in rich clusters in the same redshift range.

5.3 Stripping, Strangulation or Harassment?

Because up to now most studies have been concentrated upon rich clusters, the different mechanisms that have been proposed try to explain the transformations observed in these environments. We will review the proposed mechanisms for rich clusters, and examine the possibility of their operation in poor clusters in view of our results for the blue fraction and morphological fractions.

Several mechanisms have been proposed to explain the transformations observed in the galaxy population of rich clusters. Here I will focus on the most popular mechanisms: ram-pressure stripping, galaxy harassment, mergers and strangulation.

Ram-pressure Stripping

The suggestion of ram-pressure stripping as a mechanism to explain the transformation of galaxies in clusters, dates from the analytical work of Gunn and Gott in 1972. The motion of a galaxy through the intracluster medium (ICM), causes the formation of a pressure front that can strip gas from the disc, but how much of the gas can be stripped? Abadi et al. (1999) performed the first 3-dimensional simula-

tion of galaxies orbiting in clusters. They found that Gunn and Gott's suggestion of balancing the ram pressure with the restoring gravitational force of the disc, is successful in stripping gas from the disc. But a significant amount of gas is retained even in the case of a cluster as rich as Coma, and therefore the galaxy continues forming stars. Hence Abadi et al. (1999) concluded that ram-pressure stripping alone is not able to explain the absence of recent star formation in S0 galaxies.

But a different result is obtained when a more complex treatment of the fluid dynamics involved in the stripping process, and a more realistic treatment of the interstellar medium (ISM) are taken into account in the models (Quilis et al. 1999). The ISM is not a smooth medium but a complex one, formed by cold diffuse HI and dense molecular clouds (MC). Although Quilis et al.(1999) simulations can not resolve the MC's, they take into account the intricate structure of the gas, which has shells, bubbles and holes of different sizes. When the non-uniformity of the ISM density is included in the simulations the disc is more susceptible to the stripping process. In this case the ICM can stream through the holes, perturbing the structure of the disc and preventing gas falling back to replenish the disc. In this way all the HI content can be removed in short timescales of 10^7 years, and so, the star formation is rapidly truncated. Figure 5.2 shows how the HI component of a spiral galaxy evolves when falling into a cluster like Coma (from Quilis et al. 2000).

The efficiency of these processes increases with the density of the medium, so we would expect to observe more blue galaxies in less dense clusters where the stripping is less effective in removing the gas component. Fujita and Nagashima (1999) come to this conclusion after studying the change in the star formation rate and colours of galaxies infalling into clusters. They state that " the colour of galaxies in poor clusters is as blue as that of field galaxies if other environmental effects are not effective".

Our results do not seem to be pointing in this direction, with similar blue galaxy fractions in poor and rich clusters. If ram-pressure was the main mechanism that suppresses star formation, we would expect a big difference between the blue fractions of poor and rich clusters. This is because in clusters of galaxies the X-ray luminosity and density are related in the form $L_X \propto \rho^2$, and as previously pointed

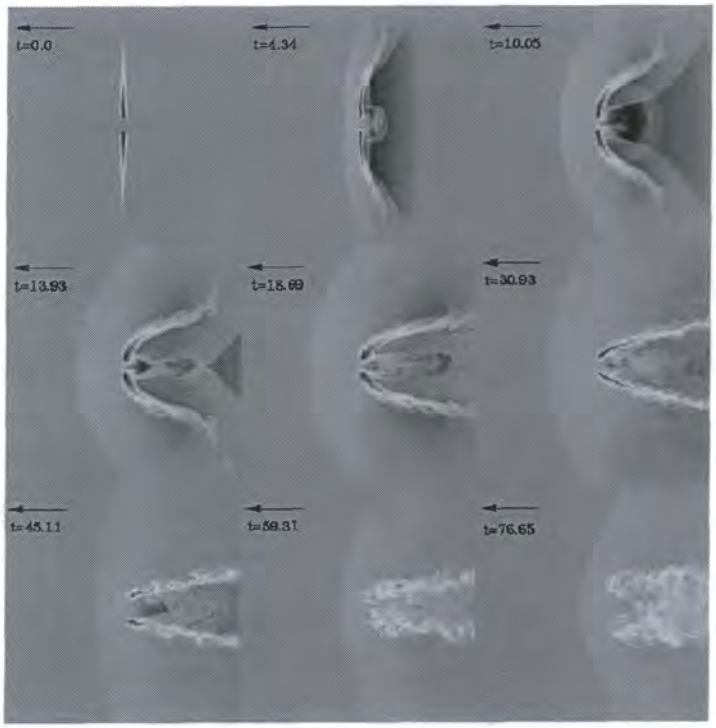

Figure 5.2: Evolution of the HI component of a spiral galaxy infalling into a cluster like Coma, from Quilis et al. 2000.

out the L_X of our poor clusters is two orders of magnitude smaller than the L_X of typical rich clusters. Therefore, since we find similar blue fraction in poor and rich clusters, we can conclude that ram-pressure stripping can not be the main mechanism responsible of the suppression of star formation.

Galaxy Harassment

"Galaxy harassment" (Moore et al. 1996, 1998) refers to rapid encounters between galaxies within a cluster, and between galaxies and tidal shocks from the cluster potential. As the new infalling spiral enters the cluster environment, it experiences several of these gravitational encounters, which leads to its transformation into an spheroidal. The time scale of this process is a few 10^9 years. Galaxy harassment is very efficient in transforming faint Sc, Sd galaxies into faint spheroidals, and therefore accounts for the observed evolution of the faint population in rich clusters. It also predicts the formation of tidal tails surrounding the remnant faint spheroidals, which are formed from the material removed from the disc. Although these are

difficult to observe because of their faintness, there is strong evidence for their existence. On the other hand, luminous spirals with more massive bulges are stable to these gravitational encounters, and although the disc can be thickened in the process, they still retain gas and continue star formation. Simulations (Moore et al. 1999) show that the different response of disc galaxies to tidal shocks depends mainly on their mass distribution, in this sense, as it can be seen if figure 5.3, low surface brightness galaxies (LSB) suffer dramatic alterations in each encounter, while high surface brightness galaxies (HSB) are more stable. After several encounters LSB galaxies can loose up to 90% of the stars from the disc and are eventually transformed into spheroidals. HSB galaxies will thicken their discs and now will be susceptible to become S0's under the effect of ram-pressure stripping.

Hence both mechanisms, stripping by the ICM and galaxy harassment, are needed to explain the transformations observed in rich clusters. But, as for ram-pressure stripping, galaxy harassment is also less effective in poor clusters since the rate of encounters is lower and therefore the timescale for the transformation will be larger. This would lead to a higher fraction of blue galaxies to be observed in less dense systems than in rich clusters.

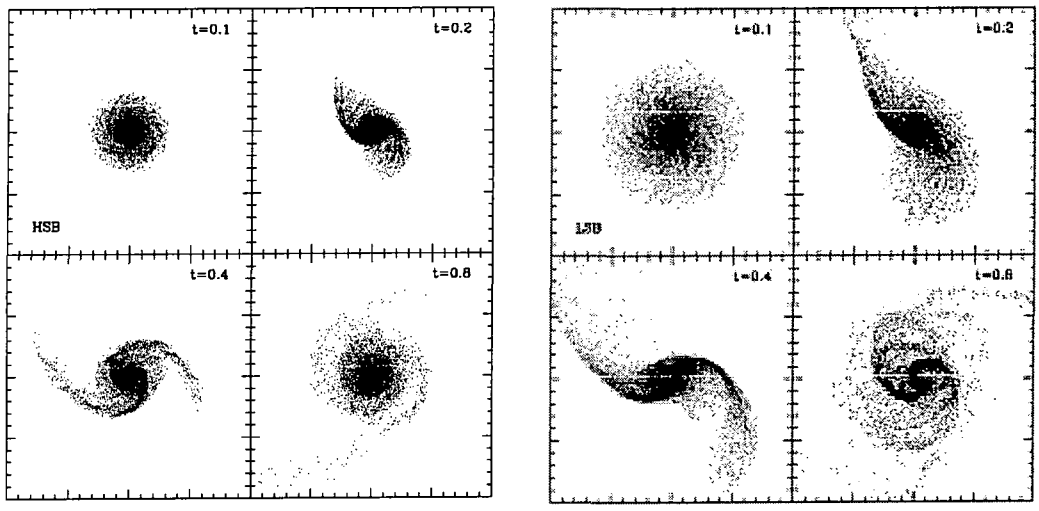

Figure 5.3: Evolution of a disc galaxy after one high-speed encounter with another galaxy. The first panel shows the evolution of a HSB galaxy, and the second panel is the case of a LSB galaxy. From Moore et al. 1999.

Interactions

Interactions between galaxies within clusters is another mechanism that can cause transformations. Strong interactions resulting in the merger of two galaxies are more effective when the relative velocity of the encounter is comparable to the internal velocities of the galaxies. In rich clusters, the relative velocity of galaxies is too high and galaxy mergers are rare (Ghigna et al. 1998). On the other hand the merger rate is estimated to be 100 times lower in rich clusters than in poor groups of galaxies (Mamon 1999). Therefore mergers could explain the blue fractions in less dense systems, but when the morphology of the population is taken into account mergers have to be excluded. This is because they would produce a population dominated by spheroidals, which does not agree with our observation of poor clusters having a population with a higher fraction of low B/T systems (see figure 4.4. Therefore mergers are not a plausible dominant mechanism to be acting in poor clusters.

Strangulation

From the above considerations we would conclude that neither ram pressure stripping, galaxy harassment or mergers are the dominant mechanisms acting in poor clusters. Then other mechanisms must be transforming the population in this environment to make the blue fraction have the low values we are finding and not affecting strongly to the morphology of the galaxies.

A mechanism that can explain our results is the so called "strangulation". In this scenario, when a galaxy from the field is accreted into the cluster its gas envelope is removed. Without this reservoir of gas, the galaxy can not refuel star formation as it would do if in the field, therefore star formation gradually declines as the galaxy consumes its gas on a timescale of a few Gyrs. This idea was first suggested two decades ago by Larson, Tinsley and Caldwell (1980), who pointed it out as an explanation for the Butcher-Oemler effect (these authors called this process "suffocation"). Further work on this topic has been performed by Balogh et al. (2000), who present a model based on this idea which successfully explains the gradients in colours and star formation rates in clusters. The model assumes that clusters are formed by the accretion of galaxies from the field, and uses N-body

simulations of cluster formation in a ΛCDM universe to determine the mass accretion rates. A gradual decline of the star formation after the galaxy is accreted to the cluster is supported by this model in order to explain the properties of the galaxy population observed in the CNOC1 sample of clusters (Balogh et al. 1999). The radial gradients observed in star formation rates and colours are therefore naturally explained as a result of the accretion history.

Strangulation will act as efficiently in poor clusters since the gas envelope is not tightly attached to the galaxy. Hence this would produce a similar blue galaxy fraction in both rich and poor cluster. The difference arises when taking into account morphologies, strangulation does not have a dramatic effect on the morphology of the infalling galaxy. Therefore in poor clusters, where other mechanisms are not effective, we expect to find a higher fraction of discs, in agreement with our findings. Whilst in rich clusters, the infalling galaxy will be also affected by ram-pressure stripping and harassment, leading to a morphological transformation into an spheroidal as we explained above. The idea that the mechanisms which cause the colour, star formation and morphology transformations, are not necessarily the same, has been already pointed out by other authors (Poggianti et al. 1999).

5.4 Conclusions

We find that the blue fractions in our poor clusters are similar to those found in X-ray selected rich clusters at similar redshifts. We have reviewed the candidate mechanisms that can cause transformations in the cluster population and have discussed them in view of our results for poor clusters. We argue that ram-pressure stripping and galaxy harassment are not the dominant mechanisms affecting the star formation in poor clusters. This is because they are less effective in less dense environments, which would produce higher blue fractions in poor clusters than in rich clusters, in contradiction of our findings of similar values in both type of clusters. We have also discussed that mergers can not be a dominant mechanism because they would not produce the high fraction of low B/T systems observed in our clusters.

We can conclude that in view of our results for poor clusters, strangulation is

likely to be the main mechanism causing the truncation of star formation, while not strongly affecting galaxy morphologies. Other mechanisms, only effective in dense environments, will be responsible of the morphological transformations observed in rich clusters.

Chapter 6

Summary and Conclusions

In this final chapter, we summarize the content of the thesis, and our results and conclusions. We also outline the future prospects for the project.

6.1 Summary of this Thesis

With the aim of understanding how the environment affects the evolution of galaxies in clusters, we have presented in this thesis photometry and spectroscopy for a sample of poor clusters of galaxies. This thesis is part of a larger project comprising nine clusters of galaxies in the redshift range 0.2 to 0.3, we have presented in this work results for four of these clusters. The original sample was selected from the Vikhlinin et al. (1998) catalogue and restricted to have an X-ray luminosity two orders of magnitude lower than the rich clusters studied so far. This is an important point to address because as we have seen in our discussion, one of the problems arising when trying to compare results from different samples is the lack of a quantitative selection criteria.

Concentrating on the subsample of four clusters presented in this thesis, we have explained how the photometry and spectroscopy have been analysed and correlated in order to create Colour-Magnitude Diagrams for these clusters. We used SPS model predictions (Arimoto and Kodama, 1997) for the slope and zero point of the red sequence to calibrate our CMD's, and found that these models are in good agreement with our results. From these diagrams, we have calculated the blue fraction of galaxies following the definition of Butcher and Oemler (1984). We find that our poor clusters have blue fraction similar to the ones found in rich clusters in the same redshift range. When comparing our sample with other X-ray selected

rich cluster samples we do not find a correlation between blue fraction and X-ray luminosity.

A key point in understanding the evolution of galaxies in clusters is the morphology of the population. HST images are also available for our sample and we have used the results of a morphological analysis performed on these images as a side project to the work presented in this thesis. These results have shown that our poor clusters are dominated by a disc population. When comparing the morphology of our cluster population with the one in rich clusters, we see that our poor clusters have a higher fraction of low B/T systems.

6.2 Summary of Conclusions

How do we interpret our results? From the findings outlined in the summary above, we conclude that the mechanism acting in poor clusters have to be able to produce a similar evolution of colours that the one observed in rich clusters, but at the same time being less effective in transforming the morphology of the galaxies. We have reviewed (section 5.3) the different mechanism that can operate in clusters, such as ram-pressure stripping, galaxy harassment, strangulation or mergers, and have discussed how their effectiveness is influenced by the environment. In view of our findings for poor clusters, we conclude that the only mechanism which is able to explain our results is strangulation. In this scenario clusters are formed by the accretion of field galaxies, which loose their gas envelopes as they enter the cluster. Galaxies in the field continue forming stars fueled by this reservoir, but in the cluster, star formation will gradually decline as the galaxy consumes the rest of its gas without having a source of replenishment. This mechanism does not have an important effect on the morphology of the galaxy, and therefore the morphological differences between the population of rich and poor cluster are also explained. In rich clusters other mechanisms, like ram-pressure stripping or harassment are effective, and will cause the observed morphological transformation of spirals into spheroidals.

A point to emphasize is that in this scenario, the mechanisms that produce the morphological and colour transformation are different ones. Strangulation is the

dominant mechanism affecting the star formation and colour of the cluster population in both rich and poor clusters. Whilst ram-pressure stripping and harassment only act in rich environments thereby producing the morphological transformation of the cluster galaxy population.

6.3 Future Prospects

As mentioned above, we have considered in this thesis four out of a sample of nine clusters, therefore the near future will be analysing the data for the rest of the clusters. This will make the results more robust in order to compare them with the existing results for rich clusters.

Naturally the next step would be expanding the poor cluster sample to a wider range of redshifts, to study the evolution in time of the galaxy population in these environments and compare it with the evolution of rich clusters.

Another interesting point would be to extend the study to poorer and poorer clusters, and finally to groups, with the aim of finding if there is a "critical" density for strangulation to start acting. Since we do not see it operating in the field and it is acting in poor clusters, it is a natural question whether its effectiveness is gradual or whether there is a "switch on" at a certain density of the environment.

Bibliography

The following abbreviations are used in this bibliography:

A&A: Astronomy and Astrophysics

A&AS: Astronomy and Astrophysics Supplement Series

AJ: The Astronomical Journal

ApJ: The Astrophysical Journal

ApJL: The Astrophysical Journal Letters

ApJS: The Astrophysical Journal Supplement

ARA&A: Annual Reviews of Astronomy and Astrophysics

JRASC: Journal of the Royal Astronomical Society of Canada

MNRAS: Monthly Notices of the Royal Astronomical Society

PASP: Publication of the Astronomical Society of the Pacific

Abadi, M. G., Moore, B. & Bower, R. G. 1999, MNRAS, 308, 947

Abell, G. O. 1958, ApJS, 3, 211

Abraham, R. G. et al. 1996, ApJ, 471, 694

Adami, C., Biviano, A. & Mazure, A. 1998, A&A, 331, 439

Adami, C., Holden, B. P., Castander, F. J., Mazure, A., Nichol, R. C. & Ulmer, M. P. 2000, A&A, 362, 825

Andreon, S. 1996, A&A, 314, 763

Andreon, S. & Ettori, S. 1999, ApJ, 516, 647

Arimoto, N. & Yoshii, Y. 1987, A&A, 173, 23

Balogh, M. L. and Morris, S. L., 2000, MNRAS, 318, 703

Balogh, M. L., Navarro, J. F. & Morris, S. L. 2000, ApJ, 540, 113

Balogh, M. L., Morris, S. L., Yee, H. K. C., Carlberg, R. G. & Ellingson, E. 1999, ApJ, 527, 54

Bertin, E. & Arnouts, S. 1996, A&AS, 117, 393

Bower, R. G., Lucey, J. R. & Ellis, R. S. 1992, MNRAS, 254, 601

Bower, R. G., Kodama, T. & Terlevich, A. 1998, MNRAS, 299, 1193

Bower, R. G., Terlevich, A., Kodama, T. & Caldwell, N. 1999, ASP Conf. Ser. 163: Star Formation in Early Type Galaxies, 211

Butcher, H. & Oemler, A. 1978, ApJ, 226, 559

Butcher, H. & Oemler, A. 1984, ApJ, 285, 426

Caldwell, N. & Rose, J. A. 1997, AJ, 113, 492

Carlberg, R. G. et al. 1997, ApJL, 476, L7

Cole, S., Aragon-Salamanca, A., Frenk, C. S., Navarro, J. F. & Zepf, S. E. 1994, MNRAS, 271, 781

Colless, M. & Dunn, A. M. 1996, ApJ, 458, 435

Couch, W. J. & Sharples, R. M. 1987, MNRAS, 229, 423

Couch, W. J., Barger, A. J., Smail, I., Ellis, R. S. & Sharples, R. M. 1998, ApJ, 497, 188

de Vaucouleurs, G. 1961, ApJS, 6, 213

Diaferio, A., Kauffmann, G., Balogh, M. L., White, S.D.M., Schade, D., Ellingson, E. 2000, MNRAS in press, preprint astro-ph/0005485

Djorgovski, S. & Davis, M. 1987, ApJ, 313, 59

Dressler, A. 1980, ApJ, 236, 351

Dressler, A. & Gunn, J. E. 1983, ApJ, 270, 7

Dressler, A. et al. 1997, ApJ, 490, 577

Dressler, A., Smail, I., Poggianti, B. M., Butcher, H., Couch, W. J., Ellis, R. S. & Oemler, A. J. 1999, ApJS, 122, 51

Ellis, R. S., Smail, I., Dressler, A., Couch, W. J., Oemler, A. J., Butcher, H. & Sharples, R. M. 1997, ApJ, 483, 582

E. Ellingson, H. Lin, H. K. C. Yee, R. G. Carlberg. 2000, ApJ in press, preprint astro-ph/0010141

Fasano, G., Poggianti, B. M., Couch, W. J., Bettoni, D., Kjærgaard, P. & Moles, M. 2000, , ApJ, 542, 673

Fujita, Y. & Nagashima, M. 1999, ApJ, 516, 619

Fukugita, M., Shimasaku, K. & Ichikawa, T. 1995, PASP, 107, 945

Ghigna, S., Moore, B., Governato, F., Lake, G., Quinn, T. & Stadel, J. 1998, MNRAS, 300, 146

Gunn, J. E. & Gott, J. R. I. 1972, ApJ, 176, 1

Hubble, E. & Humason, M. L. 1931, ApJ, 74, 43

Jørgensen, I., Franx, M., Hjorth, J. & van Dokkum, P. G. 1999, MNRAS, 308, 833

Kauffmann, G. 1995, MNRAS, 274, 153

Kodama, T. & Arimoto, N. 1997, A&A, 320, 41

Kodama, T., Arimoto, N., Barger, A. J. & Arag'on-Salamanca, A. 1998, A&A, 334, 99

Kodama, T. & Bower, R. G. 2000, MNRAS in press, preprint astro-ph/0005397

Landolt, A. U. 1992, AJ, 104, 340

Larson, R. B. 1975, MNRAS, 173, 671

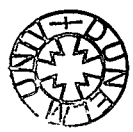

Larson, R. B., Tinsley, B. M. & Caldwell, C. N. 1980, ApJ, 237, 692

Lavery, R. J. & Henry, J. P. 1986, ApJL, 304, L5

Lavery, R. J. & Henry, J. P. 1988, ApJ, 330, 596

Lavery, R. J. & Henry, J. P. 1994, ApJ, 426, 524

Lavery, R. J., Pierce, M. J. & McClure, R. D. 1992, AJ, 104, 2067

Lilly, S. J., Tresse, L., Hammer, F., Crampton, D. & Le Fevre, O. 1995, ApJ, 455, 108

Lubin, L. M., Postman, M., Oke, J. B., Ratnatunga, K. U., Gunn, J. E., Hoessel, J. G. & Schneider, D. P. 1998, AJ, 116, 584

Mamon, G. A. 2000, ASP Conf. Ser. 197: Dynamics of Galaxies: from the Early Universe to the Present, 377

Margoniner, V. E. & de Carvalho, R. R. 2000b, ApJL in press, preprint astro-ph/0011210

Margoniner, V. E. & de Carvalho, R. R. 2000, AJ, 119, 1562

Marleau, F. R. &Simard, L. 1998, ApJ, 507, 585

Moore, B., Katz, N., Lake, G., Dressler, A. & Oemler, A. 1996, Nature, 379, 613

Moore, B., Lake, G. & Katz, N. 1998, ApJS, 495, 139

Moore, B., Lake, G., Quinn, T. & Stadel, J. 1999, MNRAS, 304, 465

Morris, S. L., Hutchings, J. B., Carlberg, R. G., Yee, H. K. C., Ellingson, E., Balogh, M. L., Abraham, R. G. & Smecker-Hane, T. A. 1998, ApJ, 507, 84

Poggianti, B. M., Smail, I., Dressler, A., Couch, W. J., Barger, A. J., Butcher, H., Ellis, R. S. & Oemler, A. J. 1999, ApJ, 518, 576

Quilis, V., Moore, B. & Bower, R. 2000, Science, 288, 1617

Rakos, K. D. & Schombert, J. M. 1995, ApJ, 439, 47

Rakos, K. D., Maindl, T. I. & Schombert, J. M. 1996, ApJ, 466, 122

Sandage, A. & Tammann, G. A. 1976, ApJL, 207, L1

Smail, I., Edge, A. C., Ellis, R. S. & Blandford, R. D. 1998, MNRAS, 293, 124

Smail, I., Dressler, A., Couch, W. J., Ellis, R. S., Oemler, A. J., Butcher, H. & Sharples, R. M. 1997, ApJS, 110, 213

Smith, S. 1936, ApJ, 83, 23

Stanford, S. A., Elston, R., Eisenhardt, P. R., Spinrad, H., Stern, D. & Dey, A. 1997, AJ, 114, 2232

Terlevich, A. I., Kuntschner, H., Bower, R. G., Caldwell, N. & Sharples, R. M. 1999, MNRAS, 310, 445

Thompson, L.A. 1986, ApJ, 306, 384

Thompson, L. A. 1988, ApJ, 324, 112

Tran, Kim-Vy H. ApJ in press, preprint astro-ph/0010278)

van Dokkum, P. G., Franx, M., Fabricant, D., Illingworth, G. D. & Kelson, D. D. 2000, ApJ, 541, 95

Vikhlinin, A., McNamara, B. R., Forman, W., Jones, C., Quintana, H. & Hornstrup, A. 1998, ApJ, 502, 558

White, S. D. M. & Frenk, C. S. 1991, ApJ, 379, 52

Yee, H. K. C., Ellingson, E. & Carlberg, R. G. 1996, ApJS, 102, 269

Zwicky, F. 1937, ApJ, 86, 217

Zwicky, F. 1957, PASP, 69, 518

Zwicky, F. & et al. 1968, California Inst. Techn., (1968)